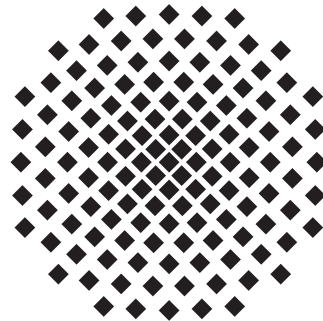


A Setup for Highly Precise Excitation and Detection of Rydberg Atoms

Masterarbeit von
Christoph Tresp
26.10.2012



Universität Stuttgart
5. Physikalisches Institut

Hauptberichter: Prof. Dr. Tilman Pfau
Mitberichter: Prof. Dr. Jörg Wrachtrup

Zusammenfassung

Rydbergatome zeichnen sich im Vergleich zu Grundzustandsatomen durch ihre starke langreichweitige Wechselwirkung aus. Diese ist besonders in ultrakalten atomaren Gasen, welche hohe Teilchendichten und geringe Teilchenabstände aufweisen, von großem Interesse. Ein häufig beschriebener Effekt ist die sogenannte Rydbergblockade. Sobald ein Grundzustandsatom mit Hilfe eines Lasers entsprechender Wellenlänge in den Rydbergzustand angeregt wird, führt die starke Rydberg-Rydberg-Wechselwirkung zu einer Verschiebung der Energieniveaus der umgebenden Atome. Dadurch ist die Frequenz des Anregungslasers nicht resonant zu diesen Atomen und es kann kein weiteres Rydbergatom angeregt werden. Innerhalb eines Volumens von einigen Mikrometer Durchmesser kann demzufolge nur ein einziges Rydbergatom angeregt werden. Die Ununterscheidbarkeit der Atome innerhalb dieses Volumens führt zu einem kollektiven Verhalten, welches beispielsweise durch eine um \sqrt{N} verstärkte Rabi-Frequenz beobachtet werden kann, wenn sich N -Atome innerhalb der Blockade befinden.

Basierend auf dieser Eigenschaft von Rydbergatomen wurden während der letzten Jahre verschiedene Konzepte vorgestellt mit dem Ziel Bauteile für Quantencomputer zu implementieren.

Im Rahmen dieser Arbeit wurde mit dem Aufbau einer neuen Apparatur zur Anregung von Rydbergatomen aus einer Wolke ultra-kalter Rubidiumatome begonnen. Der Aufbau orientiert sich an einem bereits bestehenden, soll dabei aber punktuell verbessert werden. Zu diesem Aufbau wurden zwei eigenständige Projekte beigetragen, die in dieser Arbeit detailliert erläutert werden. Dies sind zum einen der Aufbau eines hochstabilen Lasersystems zur Anregung der Rydbergatome, zum anderen eine metallische Box welche es ermöglicht während eines Experiments das elektrische Feld an der Position der Rydbergatome sehr genau zu kontrollieren.

Das aufgebaute Lasersystem für die Rydberganregung besteht aus zwei Lasern, einem Diodenlaser mit einer Wellenlänge von 780 nm und einem frequenzverdoppelten Diodenlaser, welcher bei einer Wellenlänge von 480 nm betrieben wird. Mit diesem System ist die Anregung von Rydbergatomen mittels eines Zwei-Photonen Prozesses möglich. Die vom Hersteller spezifizierte Linienbreite von 100 kHz auf einer Zeitskala von 5 μ s reichen jedoch nicht für die Beobachtung kohärenter Grundzustand-Rydberg-Dynamik aus. Dafür ist eine kombinierte Linienbreite in der Größenordnung der Linienbreite des Rydbergübergangs erforderlich, welche im Bereich von wenigen Kilohertz liegt. Aus diesem Grund wurden beide Laser nach der Methode von Pound-Drever-Hall auf einen Resonator mit hoher Finesse stabilisiert. Die so erreichte Frequenzstabilität wurde mit verschiedenen Methoden unter-

schiedlicher Güte genau untersucht.

Mittels einer Frequenzanalyse des Schwebungssignals des roten Rydberg-Lasers und eines weiteren Lasers bei gleicher Wellenlänge, welcher auf eine Rubidium-Spektroskopiezelle stabilisiert war, konnte eine maximale Linienbreite von 40 kHz auf einer Zeitskala von 700 ms gemessen werden. Eine Langzeitmessung über einen Zeitraum von 24 Stunden wies eine relative Stabilität von 600 kHz auf. Mit unserem jetzigen Wissen kann dieser Drift komplett dem auf die nicht temperaturstabilisierte Spektroskopiezelle stabilisierten Laser zugeordnet werden.

Ein niedrigeres Limit konnte durch die Nutzung eines bereits vorhandenen Selbst-Heterodyn-Interferometers bestimmt werden. Auf der bei dieser Messung relevanten Zeitskala von 52 μ s, welche einem typischen Rydberg-Experiment entspricht, lag die Linienbreite für beide Laser unterhalb der Auflösungsgrenze von 20 kHz.

Mit diesem zufriedenstellenden Ergebnis wurden die beiden Laser in den schon bestehenden Versuchsaufbau integriert. Messungen von Rydbergspektren lieferten eine Linienbreite 30 kHz. Hierbei handelt es sich jedoch immer noch um ein oberes Limit, da bei dieser Messung sowohl eine Dopplerverbreiterung von 20 kHz bei einer Temperatur von 1.3 μ K als auch eine Pulsbreitenlimitierung von 10 kHz durch die endliche Pulsdauer berücksichtigt werden muss.

Um die hohe Stabilität des aufgebauten Lasersystems im neuen Experiment voll nutzen zu können, wurde als zweites Projekt während dieser Arbeit die bereits erwähnte Box entwickelt. Diese dient dazu, die sehr sensitiven Rydbergatome, welche sich im Experiment im Inneren befinden werden, von elektrischen Feldern abzuschirmen, bzw. gezielt elektrische Felder anzulegen. Bei dem konstruierten Design wird dies durch sechs einzeln adressierbare Elektroden aus Titan erreicht, welche als Wände einer quaderförmigen Box angeordnet sind. Zusätzlich wurden in vier der Elektroden Öffnungen eingebracht, welche guten optischen Zugang gewähren. Zwei in diesen Öffnungen eingebrachte aspherische Linsen ermöglichen gleichzeitig eine sehr gute optische Auflösung von ungefähr 1 μ m. Außerdem wurde im Design die Anbringung von Ionendetektoren berücksichtigt, welche eine effiziente Detektion von Rydbergatomen durch Ionisation und anschließende Ionendetektion zulassen.

Während des Entwicklungsprozess wurde hierbei simuliert, welche elektrischen Felder im Inneren der Box erzeugt werden können. Besonderes Augenmerk lag dabei auf der Erzeugung möglichst homogener Felder um keine Verbreiterung der Linienbreite im Experiment zu erhalten.

Abstract

The interplay between high particle densities in ultra-cold atomic gases and strong long-range interactions of Rydberg atoms forms a promising candidate for applications in the field of quantum-computation. This thesis describes the setup of a new apparatus enabling to perform experiments in this field of physics.

The content of this thesis concentrates on the setup of an ultra-stable lasers system for two-photon excitation of Rubidium atoms to the Rydberg-level and the design of a metallic box offering high electric field control, both necessarily required to observe coherent dynamics of Rydberg atoms.

Declaration

I hereby declare that this submission is my own work and that, to the best of my knowledge and belief, it contains no material previously published or written by another person, except where due acknowledgment has been made in the text.

Christoph Tresp
Stuttgart, October 28, 2012

Contents

1. Introduction	9
2. Setup of the new Rydberg apparatus	11
2.1. MOT-Chamber	12
2.2. Magnetic transport	13
2.3. Experiment chamber	14
3. Rydberg excitation system	17
3.1. Rydberg excitation in cold gases	17
Lifetime of Rydberg atoms	18
Two-photon Rydberg excitation	20
3.2. Laser stabilization	22
3.2.1. Introduction to optical resonators	22
Basic resonator formulas	23
Mode matching	24
3.2.2. Pound-Drever-Hall technique	26
3.3. Experimental setup	29
3.3.1. Optical setup	29
Setup of the red 780 nm laser	29
Setup of the blue 480 nm laser	29
Setup of the reference cavity	30
3.3.2. Electronic setup	33
3.4. Characterization and optimization of the stability	35
3.4.1. Characterization of the resonator	35
3.4.2. Feedback loops	39
Characterization of the laser electronics	42
Characterization of the feedback-loop	45
3.4.3. Measurement of the laser linewidth	48
Heterodyne linewidth measurement by a beatnote with a second laser	48
Measurement of the long-time stability	50
Linewidth measured by a delayed self-heterodyne interferometer . .	50
3.4.4. Rydberg-spectroscopy in the existing setup for Rydberg experiments	54
Spectroscopy on the 44d-state	55
Spectroscopy on the 35s-state	56

4. Rydberg box	59
4.1. Rydberg atoms in electric fields	59
4.1.1. Stark-shift of Rydberg states	59
4.1.2. Field ionization of Rydberg atoms	60
4.2. Design of the experiment box	62
4.2.1. Electric fields inside a metallic box	63
4.2.2. Design of the box	65
4.2.3. Simulations of the electric field control	67
Simulations of electric fields used to shift the energy levels	67
Simulations of electric fields used to ionize Rydberg atoms	69
5. Summary and Outlook	73
A. Modematching to the cavity	75
B. Electronics for scanning the laser	77
C. Excitation scheme for Rydberg excitation	78
Bibliography	79

1. Introduction

With the explanation of the numerous lines in the excitation spectrum of hydrogen by Johannes Rydberg in 1888, the highly excited atoms attracted the notice of scientists for the first time [1].

In today's atomic physics Rydberg-atoms play a unique role due to their strong long-range interactions based on their high polarizability. Especially, the ability to turn the interaction on and off and to switch sign from attractive to repulsive provides diverse applications [2]. Besides other approaches like the usage of ions [3], NV-centers [4] or Quantum-Dots [5], and in combination with high particle densities in ultra-cold atomic gases, Rydberg-atoms are a promising candidate for applications in quantum-computation [6].

Different schemes for the implementation of gates for quantum-computation based on interaction between Rydberg-atoms were proposed at the beginning of this century [7, 8]. The core of these proposals is the so-called Rydberg-blockade effect [8]. As soon as one atom is excited to a Rydberg-state, the Rydberg-levels of the neighboring atoms are shifted due to the strong interaction, preventing them from excitation by the driving laser. Thus, within a radius of typically several micrometers only one Rydberg-atom can be excited. The indistinguishability of the involved atoms causes a collective behavior, described in the "Superatom"-model [9]. The collective nature of the superatom results in an enhancement of the Rabi frequency driving the transition from ground state to collective single-excitation state by the excitation laser by the square root of the number of atoms in the blockaded sphere. In 2004 the collective enhancement was proven at low densities first [10] and later in the high density regime [11]. Only recently enhanced Rabi-oscillations in ensembles with more than 100 atoms were demonstrated [12].

Various experiments triggered by these theoretical predictions and experimental observations yielded new important results. Thus, for example the first experimental realization of a quantum gate based on Rydberg-atoms was demonstrated in 2009 [13, 14].

All these results emphasize that Rydberg-atoms can serve as fundamental component for applications in quantum-computation, offering the possibility to build required single-photon-sources [15], single-photon absorbers [16] and a quantum repeater [17, 18] for quantum-communication over long distances.

The purpose of quantum-simulators is to replicate the dynamics of any quantum-mechanical system. Goal of these studies is to solve problems which are intractable on classical computers. A universal quantum simulator for spin-models involving n-body interactions based on Rydberg-atoms has already been proposed, but could not be experimentally realized so far [19].

About this thesis

In the scope of this thesis the setup of a new apparatus for experiments on Rydberg-atoms in ultra-cold atomic gases has been initiated, harking back to the experiences made with an already existing setup [20]. The outstanding results of the experiments performed with the existing machine contributed significantly to the understanding of the interactions of Rydberg atoms. Among these results are the first excitation of Rydberg atoms in a Bose-Einstein condensate [21], the experimental observation of the blockade effect [22] and novel Rydberg ground state molecules of extreme size [23]. In the latest results the coherent switching between van-der-Waals interaction and resonant dipole-dipole interaction could be demonstrated [24, 25].

The new apparatus combines the existing knowledge of working with ultra-cold Rydberg atoms with various new aspects. Firstly, optical resolution smaller than typical blockade diameters allows for addressing individual superatoms and direct observation of their collective dynamics. Previously, the resolution was not high enough to address one single superatom. Different numbers of atoms in the addressed superatoms therefore led to a dephasing, washing out the Rabi oscillations. In the new experiment good optical access and high resolution are provided by a glass cell and aspheric lenses mounted inside the vacuum.

Further design goal of the new machine are extremely precise electric and magnetic field control as well as high stability of the laser system for the Rydberg-excitation. Fluctuations of external field and excitation lasers could be identified as sources of decoherence in the existing experiment, so that these improvements will result in longer coherence times of the Rydberg superatoms. Realizing a QUIC-trap configuration for the magnetic trapping of the ultra-cold atoms will give higher stability of the magnetic fields and moreover reduce the cycle time of the experiment dramatically. The installation of a metallic box inside the glass cell will provide extremely precise electric field control. Mounted to this box are two ion-detectors, allowing the detection of ionized Rydberg-atoms. Optimization of the guiding electric fields and the detector placement will improve the detection efficiencies significantly compared to the existing setup.

While this thesis gives a overview of the general setup of the new apparatus, two subjects are discussed in detail in this thesis. Firstly, the setup of a ultra-stable laser system making observation of coherent Rydberg dynamics observable is described. This part includes both a detailed description and characterization of the setup used to stabilize the frequencies of the two involved lasers to a reference resonator. The second part discusses the design and construction of the experiment box used to provide accurate electric field control during the experiment. To manifest that this box enables precise shifting of atomic levels of the Rydberg-atoms by the Stark-effect and high efficiencies for ion-detection by the mounted ion-detectors can be achieved, different simulations on the electric fields inside this box are discussed.

2. Setup of the new Rydberg apparatus

The already existing Rydberg experiment in the institute of Professor Tilman Pfau did not only produce many outstanding results, but also important experiences how to improve the apparatus. For this reason, the setup of a completely new system was started in summer 2011.

Goal of the experiments is to examine different aspects of Rydberg atoms excited from an ultra-cold ensemble of atoms. Therefore the new apparatus has to fulfill several requirements, resulting in a complex construction. For the creation of ultra-cold atomic gases a vacuum chamber providing ultra-high vacuum is essential, granting a high lifetime of the atomic ensembles. Additionally narrow lasers are necessary for both cooling and trapping of the neutral atoms and the excitation of Rydberg atoms. The setup of the MOT laser system is described in [26], the latter ones are described in this thesis in chapter 3. Finally high control on magnetic and electric fields is inevitable for precise manipulation and detailed analysis of Rydberg atoms.

For the combination of both ultra high vacuum and fast repetitions rates of the experiment, we decided to build a setup consisting of two chambers, a steel chamber and a glass cell. A rubidium reservoir is connected to the steel chamber allowing fast loading of a magneto-optical trap. Steel chamber and glass cell are connected to each other by a thin tube acting as differential pumping stage, leading to a decrease in pressure by more than two orders of magnitude. Using a magnetic transport the atoms trapped into the MOT are transported in the glass cell and loaded into a magnetic trap. There the atoms are further cooled to obtain atomic clouds with ultra-low temperatures or even quantum degenerate gases. Setup and principle of the different stages are described in more detail in sections 2.1 to 2.3.

Of course this is not the only scheme to work with ultra-cold atomic ensembles. Other approaches would be for example to use a single chamber and load the MOT with an atomic beam decelerated in a Zeeman-slower or to use a push beam instead of the magnetic transport. The reason for our choice of a two-chamber setup with magnetic transport is the good compromise between complexity and stability of the setup, already demonstrated in various experiments [27, 28].

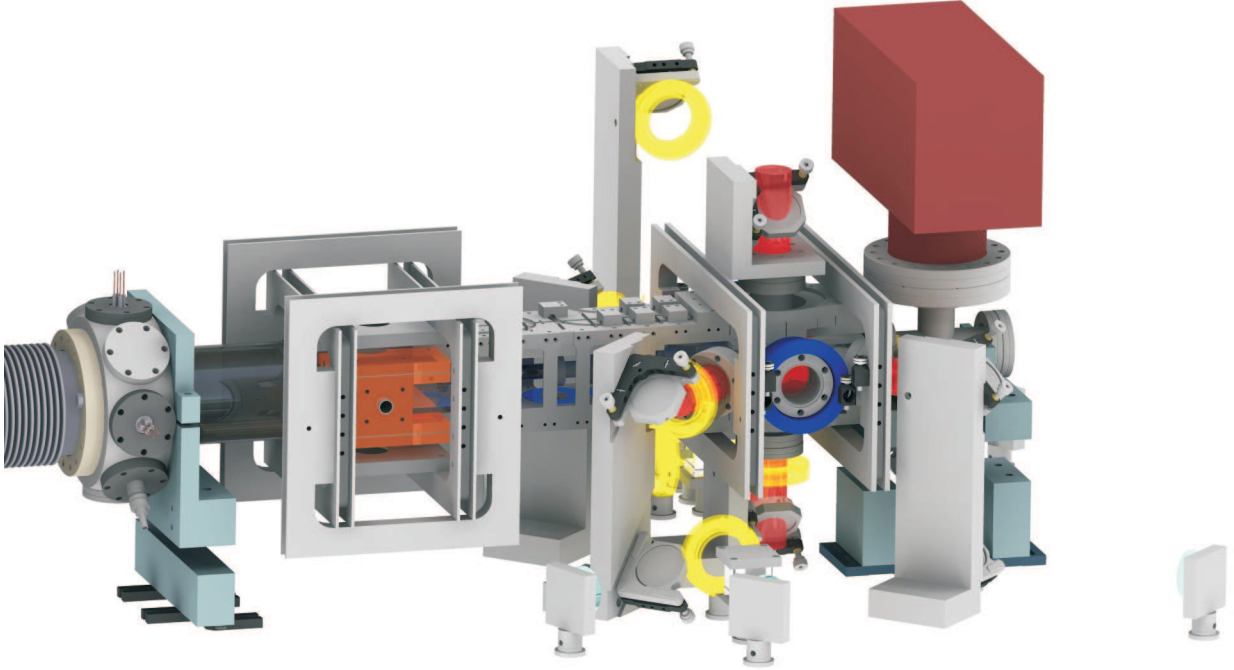


Figure 2.1.: Engineering drawing of the complete vacuum chamber used to capture and cool atoms.

2.1. MOT-Chamber

The first step in the preparation of ultra-cold atomic gases is a magneto-optical trap (MOT) [29]. By several processes of absorption and spontaneous emission of photons the atoms are decelerated. An additional magnetic quadrupole field created by a pair of coils in anti-Helmholtz configuration results in spatial dependent confinement.

To provide the required laser beams from all directions the MOT chamber has optical access through six windows, supporting confinement in all spatial directions. Using large beams with a diameter of 2 inch allows to capture up to 10^9 atoms.

The Rubidium required to load the MOT is provided by a reservoir containing 5 g of elemental rubidium. In between reservoir and MOT-chamber a valve is mounted to control the flow of rubidium atoms. Depending on the aperture of the valve the pressure in the chamber settles to an equilibrium value caused by the vapor pressure of rubidium and the throughput of the mounted ion-pump. To achieve fast loading while still retaining sufficient lifetime in this region, the background Rubidium pressure in the MOT area is regulated to

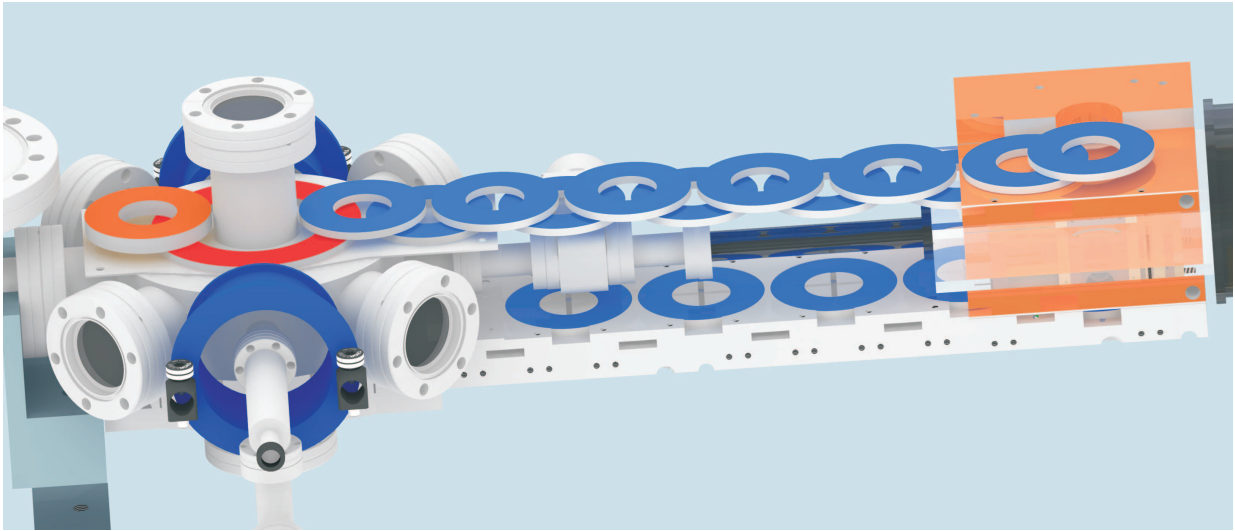


Figure 2.2.: Engineering drawing of the magnetic transport

10^{-9} mbar.

2.2. Magnetic transport

The principle of the magnetic transport is based on the Zeeman-splitting of the atomic levels [28]. Due to the dependence of the energy of the magnetic sub-states on the magnetic field they can be trapped in the extremum of a magnetic field. As in free space no local maximum of the magnetic field can exist, only the low-field seeking states, i.e. states which are shifted to positive energy in a finite B-field, can be trapped. Consequently, once a cloud of atoms is trapped in the minimum of a magnetic field its position can be changed by shifting the position of the minimum of the magnetic field sufficiently slow such that the atoms can follow the changing trapping potential adiabatically. For this purpose twelve pairs of coils in anti-Helmholtz configuration are mounted above and below the route between MOT-chamber and the glass cell. By applying currents in a certain sequence, the minimum of the magnetic field can be continuously shifted along the coils. Therefore the atoms can be transported from the MOT chamber to the glass cell. The setup of the magnetic transport is shown in figure 2.2. All coils for the magnetic setup are mounted in aluminium holders leading away the dissipated heat.

For reaching high efficiencies in the magnetic transport, the following scheme is applied. After loading the atoms into the MOT, they are further cooled by optical molasses cooling. With optical pumping the sample is spin-polarized into a low-field seeking magnetic sub-level of the ground state. Afterwards the atoms are loaded into a magnetic trap. Therefore a high current is applied to the MOT-coils. By applying currents to the transport coils in a certain sequence, the atoms are then transported to the glass cell.

2.3. Experiment chamber

The actual Rydberg experiments take place in a glass cell providing good optical access. A second advantage of a glass cells over a steel chamber is the opportunity of building a more compact design.

In the last step of the magnetic transport, the quadrupole trap generated by the final coil pair is changed into a Ioffe-type trap by ramping up a current in an additional coil mounted perpendicular to the Anti-Helmholtz pair [30]. In contrast to a quadrupole-trap the QUIC (quadrupole-ioffe-configuration)-trap generates a non-vanishing offset field at the center of the trap, which is necessarily required to avoid losses due to Majorana spin-flip transitions in ultra-cold samples [31].

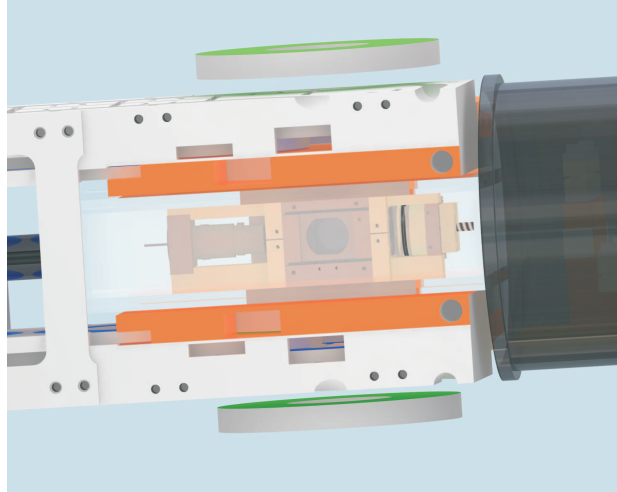


Figure 2.3.: Engineering drawing of the experiment chamber

The choice for this kind of trap has several reasons. First, in contrast to an optical dipole-trap, magnetic traps allow to change the shape of the trap by applying different currents. Therefore it is for example possible to quickly cool the atoms in a compressed trap and expand the cloud afterwards by lowering the trapping frequencies. In contrast to other approaches for magnetic traps the QUIC-trap allows smaller construction and operation with moderate currents (40 A). To get rid of the still released heat, all coils are mounted in water cooled copper holders. Besides the coils for the QUIC-trap further offset-coils are mounted around the chamber allowing to move the trapping position in all three spatial directions.

After having loaded the atoms into the QUIC-trap further cooling by evaporative methods [32] completes the preparation of ultra-cold atoms.

For the following Rydberg experiments a further box is placed in the glass cell with its center coinciding with the position of the atoms. The purpose and the properties of this experiment box are described in detail in chapter 4. Briefly summarized its functions are accurate electric field control at the position of the sensitive Rydberg atoms and the

2. Setup of the new Rydberg apparatus

opportunity for counting ionized Rydberg atoms by connected ion-detectors (multi-channel plate and channeltron). A common experiment sequence consists of optical excitation of Rydberg atoms and subsequent ion detection after ionization. The signal of the detected ions allows to draw conclusions on the Rydberg atoms.

3. Rydberg excitation system

For the excitation of the Rubidium atoms to the Rydberg level, a laser-system had to be built. This chapter will describe the demands on the excitation system in a cold Rydberg experiment as well as its experimental realization. It follows a detailed characterization of the built setup, showing that all requirements are fulfilled.

3.1. Rydberg excitation in cold gases

Taking a look at the level scheme of Rubidium, it becomes clear that there are many different ways to excite Rubidium ground state atoms to the Rydberg level, either directly or by multi-photon transitions. Figure 3.1 shows three different possibilities to reach the Rydberg level.

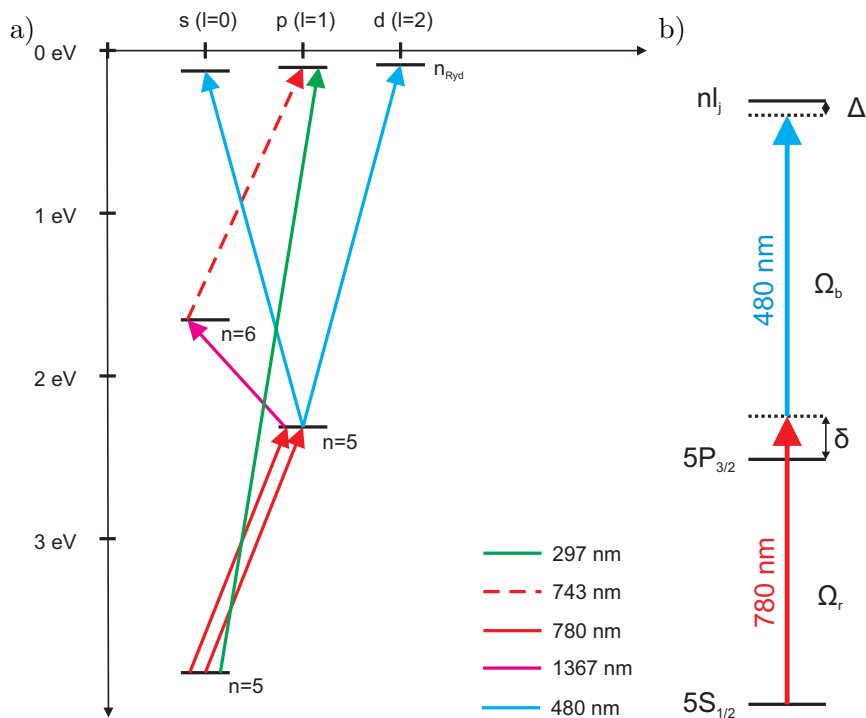


Figure 3.1.: Different approaches for optical Rydberg excitation of Rubidium atoms via single-photon, two-photon or three-photon excitation a) and detailed illustration of the used two-photon excitation scheme b).

3. Rydberg excitation system

The first option is to use one single laser operating at a wavelength of 297 nm. This solution has the advantage that only one single laser is required, but on the other hand lasers with this wavelength are difficult to produce and the excitation lines are fully Doppler-broadened.

Another approach is to use a two-photon excitation via an intermediate level. One solution to do so is to use a red 780 nm laser for the first step to the 5P intermediate level and a blue 480 nm laser for the second step to the Rydberg level. The benefit of this solution for the Rydberg excitation is the availability of these lasers and the possibility to partially compensate for the Doppler-shift by counter propagating beams. The disadvantage of this scheme is the need of two lasers which makes the setup more complex.

Finally, with a reasonable number of lasers it is also feasible to use a three photon-excitation scheme with two intermediate levels. By choosing the right direction of the beams relative to each other, three-photon excitation offers the possibility to fully compensate for Doppler-broadening and in addition one does not suffer from recoil [33]. Compared to the two-photon excitation the setup of the laser system is even more complicated.

Lifetime of Rydberg atoms

One of the requests on the laser system is imposed by the lifetime of the considered Rydberg state defining the linewidth of the excitation. For resolving the linewidth of an atomic transition the frequency inaccuracy of the laser frequency has necessarily to be smaller than the linewidth.

For a two-level system the lifetime of the excited state can be expressed by the Einstein A-coefficient for spontaneous emission of a photon as

$$\frac{1}{\tau_{if}} = A_{if} = \frac{\omega_{if}^3}{3\pi\epsilon_0\hbar c_0^3} |\langle f | \mathbf{er} | i \rangle|^2, \quad (3.1)$$

where ω_{if} is the transition frequency and $\langle i | \mathbf{er} | f \rangle$ the transition dipole moment for the transition from state $|i\rangle$ to state $|f\rangle$. In the case of Rydberg atoms it is not sufficient to take only one final state into consideration, as the Rydberg state can normally decay to different states. Therefore one has to sum up the contributions of all involved transitions, leading to

$$\frac{1}{\tau_{n,l}^{n',l'}} = \sum_{n',l'} A_{n,l}^{n',l'}. \quad (3.2)$$

The Einstein A-coefficients do not only include the transition dipole moment, but also the transition energies $\omega_{n,l}^{n',l'}$ to the power of three. The values for transitions between neighboring Rydberg levels are about 100 GHz and $1000ea_0$ the values for the level spacing and the dipole matrix element, respectively. For a decay to the ground state on the other hand, the level spacing is about 600 THz and the transition dipole moment approximately

3. Rydberg excitation system

0.01 ea_0 . This means, that the strongest contribution to the lifetime comes from the decay of Rydberg atoms to the ground state.

The radiative lifetime can be expressed by an empirical formula [34]

$$\tau = \tau_0 \cdot n^{*\alpha}. \quad (3.3)$$

From the comparison to experimental results the values for τ_0 and α can be obtained.

	τ_0 [μ s]	α
s-state	1.43	2.94
p-state	2.76	3.02
d-state	2.09	2.85

Besides the spontaneous decay to the ground state there is a second mechanism limiting the lifetime of Rydberg atoms. This occurs when the predominant modes of the blackbody spectrum of the environment become equal to the splitting of the energy difference between neighboring Rydberg levels. In this case stimulated emission to other Rydberg levels occurs reducing the lifetime.

The probability $W_{n,l}^{n',l'}$ for a blackbody induced transition from a state n,l to a state n',l' can be calculated by the Einstein coefficient and the number of photons per mode, given by the Planck-distribution

$$W_{n,l}^{n',l'} = A_{n,l}^{n',l'} \cdot \frac{1}{\exp(\omega_{n,l}^{n',l'}/kT) - 1}. \quad (3.4)$$

From this equation follows the decay rate Γ_{BBR} by summing over all contributing Rydberg states

$$\Gamma_{BBR} = \frac{1}{\tau_{BBR}} = \sum_{n',l'} A_{n,l}^{n',l'} \cdot \frac{1}{\exp(\omega_{n,l}^{n',l'}/kT) - 1}. \quad (3.5)$$

In consequence the total lifetime of Rydberg atoms is given by

$$\tau(n,l) = \left[\frac{1}{\tau_{rad}(n,l)} + \frac{1}{\tau_{BBR}(n,l)} \right]^{-1}. \quad (3.6)$$

In figure 3.2 both radiative lifetime and BBR-included lifetime of Rydberg atoms are shown. The lifetimes including BBR were calculated by an expression determined in [35].

Due to the uncertainty relation the lifetime results in a finite linewidth obeying the relation

$$\delta\nu = \frac{1}{2\pi\tau}. \quad (3.7)$$

Inserting the values for the lifetimes according to figure 3.2 yields to natural linewidths of about 1 kHz to 10 kHz for Rydberg-states between $n \approx 80$ and $n \approx 35$, which sets quite stringent demands on the frequency stability of the Rydberg excitation lasers.

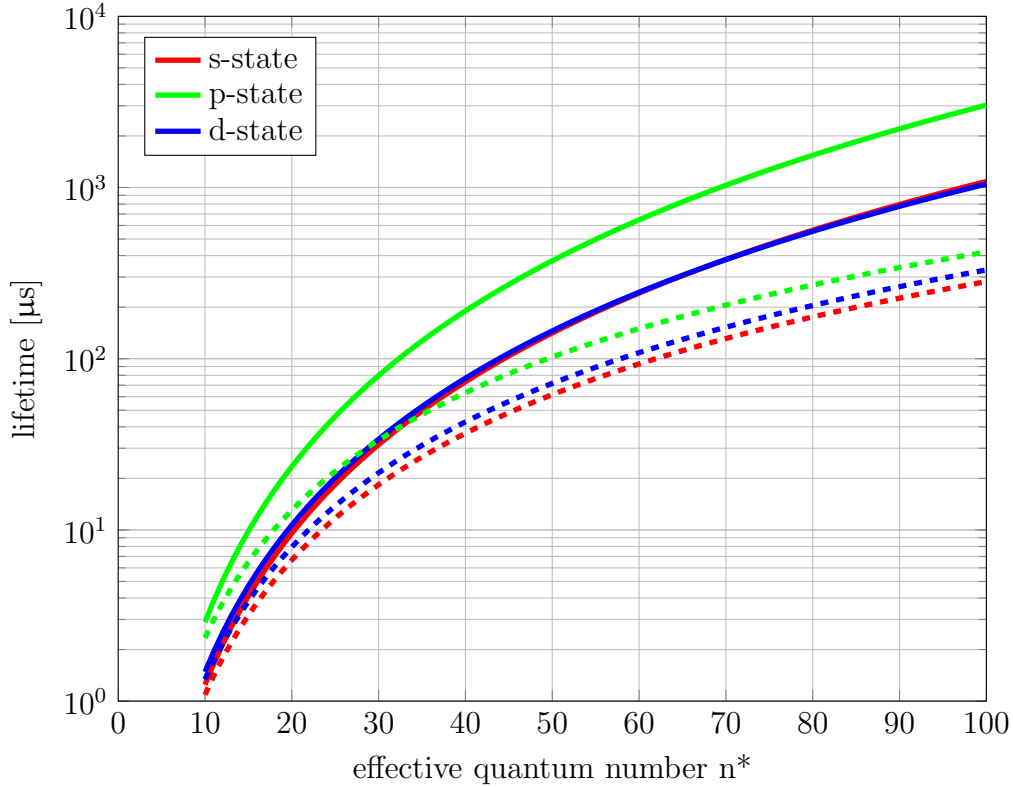


Figure 3.2.: Lifetime dependence on the principal quantum number n^* for Rydberg atoms in s-states (red), p-states (green) and d-states (blue). The solid lines represent the calculated lifetime of Rydberg atoms due to spontaneous scattering to lower lying levels. The dashed lines include also BBR. For increasing quantum number BBR decreases the lifetime considerably.

Two-photon Rydberg excitation

For our experiment we have chosen the two-photon excitation scheme depicted in figure 3.1 b), starting from the $5S_{1/2}$ -level via the intermediate $5P_{3/2}$ -level to the Rydberg level. To obtain a coherent excitation to the Rydberg level one both has to avoid a population of the intermediate level and the Rabi frequency of the transition has to be larger than the decay rate of the Rydberg level [36]. The first constraint can be achieved by choosing a large detuning δ to the intermediate level compared to the single photon Rabi frequencies Ω_r and Ω_b . For the second condition one has to take into consideration the effective Rabi frequency for the two-photon transition, which is given by

$$\Omega_{\text{eff}} = \sqrt{\frac{\Omega_r^2 \Omega_b^2}{4\delta^2} + \Delta^2}, \quad (3.8)$$

where Δ is the total detuning of the two-photon transition. In principal the effective Rabi frequency can be increased by enlarging the two-photon detuning or increasing the single-

3. Rydberg excitation system

photon Rabi frequencies. However enlarging Δ is not the method of choice since this leads to a decreasing fraction of atoms in the Rydberg state.

For large detuning compared to the single photon Rabi frequency the scattering rate from the intermediate 5P level is given by

$$\Gamma_s \approx \frac{\Gamma\Omega_r^2}{4\delta^2}. \quad (3.9)$$

Consequently, the maximal Rabi frequency Ω_r of the red excitation laser is limited due to scattering, which causes loss of atoms as well as significant heating of the ultra-cold ground-state atoms. Increasing Ω_{eff} is therefore preferably done by increasing the Rabi frequency of the blue laser.

As of today 480 nm lasers with a power of about 150 mW are available. As an illustrative example, let us consider a blue beam focused to a waist of 10 μm , which is the order of magnitude for the Rydberg-blockade radii. The transition dipole moment from the intermediate-state to the Rydberg-state scales with $C_l \cdot n^{*-1.5}$, where C_l is 4.502 ea_0 for S-states and 8.457 ea_0 in the case of D-states [37]. In particular, for the 50S-state for example, it has a value of $\mu_b = 0.0140 ea_0$. Thus the resulting Rabi frequency is

$$\frac{\Omega_b}{2\pi} = \frac{\mu_b}{\hbar\omega_0} \sqrt{P\epsilon_0 c\pi^3} = 24.2 \text{ MHz}. \quad (3.10)$$

For the $5S_{1/2} \rightarrow 5P_{3/2}$ transition the transition dipole-moment $\mu_r = 4.227 ea_0$ [38] is two orders of magnitude larger. With 10 μW laser power and a waist of 10 μm this results in a Rabi frequency of

$$\frac{\Omega_r}{2\pi} = 59.6 \text{ MHz}. \quad (3.11)$$

The effective two-photon Rabi frequency for these parameters, $\delta = 400 \text{ MHz}$ and vanishing two-photon detuning Δ is

$$\frac{\Omega_{\text{eff}}}{2\pi} = 1.8 \text{ MHz}, \quad (3.12)$$

which is much higher than the decay rate of about 10 kHz of the Rydberg atoms, making coherent groundstate-Rydberg state dynamics possible.

is well higher than the decay rate $\Gamma = \frac{1}{\tau}$ which is in the order of 10 kHz for Rydberg atoms.

A laser-system for two-photon Rydberg excitation should therefore fulfill two conditions to allow coherent excitation. On the one hand the linewidth of the laser has to be in the kHz-regime and on the other hand enough power in the second excitation step is required.

3.2. Laser stabilization

Although the ideal laser emits an electromagnetic wave with one well defined frequency, quantum-fluctuations [39] in the active laser medium and technical noise lead to a finite linewidth of the output spectrum. A possibility to describe noise in the laser field is to add a random phase $\varphi(t)$ in the electromagnetic field describing the laser field. It can be shown that quantum-fluctuations lead to a frequency-independent noise, while the technical noise, resulting from drifts of the laser-resonator for example, decreases with higher frequencies [40]. The task of laser stabilization is thus to limit the technical noise.

The lasers used for the Rydberg excitation are so called external-cavity diode lasers (ECDL)¹. These types of lasers consist of a semiconductor laser-diode, which is temperature stabilized by a thermo-element, and an external grating as refractive element, which is used to couple one frequency component of the emitted light back into the laser diode to amplify exactly this frequency. The frequency of the laser can be tuned by changing the temperature of the thermo-element, the current of the laser diode and the angle of the grating.

In order to actively stabilize the lasers output frequency to a narrow linewidth, one has to find an optical element, which produces a dispersive signal depending on the laser frequency. Such elements can be designed for example with Rubidium vapor cells [41] or optical cavities (see section 3.2.2 for more information). With a suited controller this dispersive signal can be fed back to the laser and therefore the output frequency can be stabilized. As the feedback of changes in the laser diodes temperature have a large time constant, the voltage of the thermo-element is thereby normally kept constant. Instead, to compensate for slow drifts, the angle of the grating is changed by a piezoelectrical element, or in order to suppress fast drifts, the current of the laser diode is modulated.

The quality of the frequency stabilization of a laser depends on different parameters. First, the dispersive signal created by the frequency reference necessarily has to have steep slope and a high frequency stability. Secondly, the electronics which are used to stabilize the laser frequency onto the reference needs a bandwidth that is high enough to compensate for drifts over a large frequency range and finally it is important, that the components of the laser can be modulated fast enough.

3.2.1. Introduction to optical resonators

High finesse resonators provide extremely narrow and stable references. By choosing a suitable design it is possible to create an error signal at any wavelength. Additionally, the linewidth can be narrowed by using high-quality mirrors. Using atoms as reference instead, one is always limited by the natural linewidth defined by the lifetime. A further advantage of optical resonators is the possibility to stabilize different wavelengths to one single cavity. For this reason we decided to stabilize our Rydberg-lasers to an optical cavity.

¹Toptica DLpro series

Basic resonator formulas

A simple optical resonator consists of two mirrors, which are mounted face to face to each other. By this arrangement, light that is coupled into the resonator reflects back and forth between the mirrors several times. When the distance between the mirrors is an integer multiple of $\frac{\lambda}{2}$ the wave trains inside the cavity interfere constructively with each other. This causes a maximum in intensity transmitted through the cavity. Detailed analysis of the transmission function [42] leads to the electric field transmittance coefficient

$$\mathcal{T}(\nu) = \frac{E_{\text{trans}}}{E_0} = \frac{1 - r^2}{1 - r^2 e^{i\frac{4\pi L\nu}{c}}} \quad (3.13)$$

as well as to the reflection coefficient

$$\mathcal{R}(\nu) = \frac{E_{\text{ref}}}{E_0} = \frac{r(e^{i\frac{4\pi L\nu}{c}})}{1 - r^2 e^{i\frac{4\pi L\nu}{c}}}. \quad (3.14)$$

In these equations r is the reflectivity of the electric field at the mirrors, ν the frequency of the light and L the length of the cavity.

From this one can calculate the reflected and transmitted intensity, which is proportional to the square of the absolute value of the electric field. The resulting intensity of transmitted light is

$$T(\nu) = I_0 \frac{1}{1 + \frac{4R}{(1-R)^2} \sin^2(2\pi \frac{L}{c} \nu)}, \quad (3.15)$$

where I_0 is the intensity of the light with frequency ν coupled into the cavity, L the length of the cavity and R the reflectivity of the mirrors.

In figure 3.3 the frequency dependence of the transmission through the cavity is shown for different reflectivities of the mirrors. From equation 3.15 one can find two characteristic quantities, which can also be seen in the figure. These are the width of the transmission peaks and the distance between two peaks in frequency space. A maximum in transmission occurs when the argument of the sine in equation 3.15 becomes a multiple of 2π . The free-spectral range, i.e. the distance in frequency between two peaks, is therefore given by

$$\Delta\nu = \nu_{n+1} - \nu_n = \frac{c}{2L} \cdot (n+1) - \frac{c}{2L} \cdot n = \frac{c}{2L}. \quad (3.16)$$

As the speed of light is a fixed constant, the separation of two transmission maxima is determined only by the distance L between the mirrors. So, when a cavity is used as a frequency reference, the distance between the mirrors has to be fixed with high precision. The acceptable jitter in the distance between the mirrors can be determined by a short estimation. From the condition $L = n \frac{c}{2\nu}$ it follows

$$\Delta L = \frac{\Delta\nu}{\nu} \cdot L. \quad (3.17)$$

For $L = 10$ cm like it is used in our setup (see section 3.3.1) and a stability of around

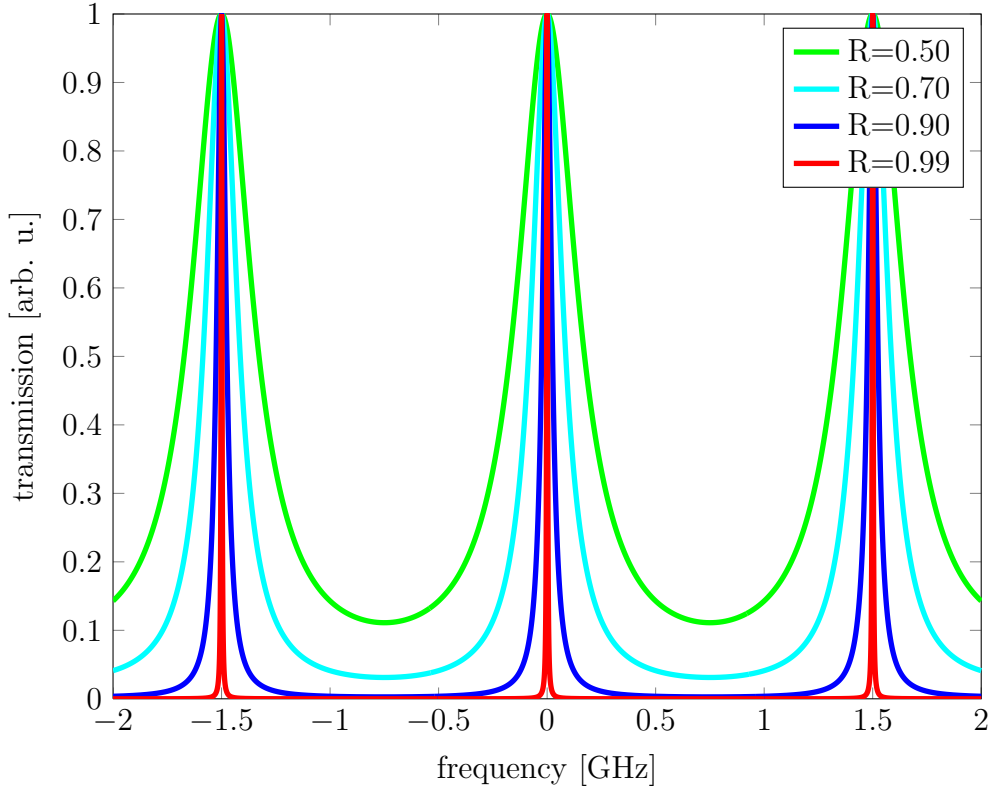


Figure 3.3.: Frequency dependence of the transmission signal [arb. u.] of an optical cavity for different reflectivities.

10 kHz a stability of approximately 1 pm is required.

The FWHM of a transmission peak can be found under the approximation $R \gg 1 - R$ to be

$$\nu_{1/2} = \frac{c}{2\pi L} \frac{1 - R}{\sqrt{R}}. \quad (3.18)$$

This means, that for a given length L , the transmission width can be decreased by increasing the reflectivity of the mirrors.

The ratio of free-spectral range and width of the peak is often referred to as Finesse \mathcal{F} of a cavity and given by

$$\mathcal{F} = \frac{\Delta\nu}{\nu_{1/2}} = \frac{\pi\sqrt{R}}{1 - R}. \quad (3.19)$$

Mode matching

The properties of an optical resonator described in 3.2.1 were calculated by describing and interfering the fields as planar waves. This assumption is correct as long as both mirrors

are planar. For other geometries of the mirrors the spatial distribution of the fields inside the resonator is depending on the shape and the arrangement of its mirrors. In the case of a cavity consisting only of planar and spherical elements the solutions for the field are the well known Hermite-Gaussian beams [43].

To reach the optimal coupling to the cavity in the experiment it is important to match the beam coupled into the cavity to the spatial field distribution which is supported by the cavity. In figure 3.4 the cross section of such a Gaussian beam and its important properties are illustrated.

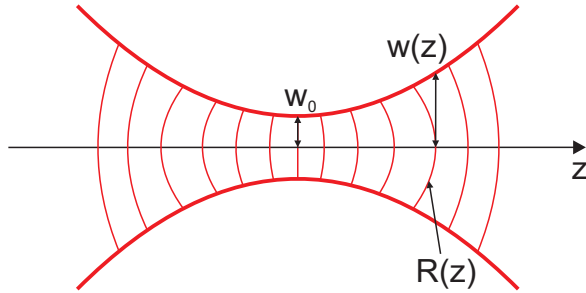


Figure 3.4.: Schematic drawing of the transverse profile of a Gaussian beam.

The intensity along the transverse profile of a Gaussian beam is described by

$$I(r, z) = I_0 \left(\frac{w_0}{w(z)} \right)^2 \exp \left(-\frac{2r^2}{w(z)^2} \right). \quad (3.20)$$

Here z is the axis along the beam and $w(z)$ is the radius of the beam in the transverse direction r , defined as the point at which the intensity is $\frac{1}{e^2}I_0$. The radius $w(z)$ at any position along the beam is related to beam waist w_0 , i.e. the minimal beam radius, according to

$$w(z) = w_0 \sqrt{1 + \left(\frac{z}{z_R} \right)^2}. \quad (3.21)$$

The quantity z_R , denoted as Rayleigh range, defines the distance at which $w(z)$ is equal to $\sqrt{2}w_0$, it can be expressed by

$$z_R = \frac{\pi w_0^2}{\lambda}. \quad (3.22)$$

The final parameter which is of great importance is the curvature of the wavefront

$$R(z) = z \left[1 + \left(\frac{z_R^2}{z^2} \right) \right]. \quad (3.23)$$

For achieving the best coupling to the cavity the curvatures of the incident Gaussian beam at the position of the mirrors have to be equal to the radius of the mirror. Only in this

case the beam is reflected back into itself. Otherwise intensity gets lost due to diffraction, absorption or excitation of higher transversal modes.

In addition, the resonance frequencies change compared to the calculation with planar waves, as the additional Gouy-phase has to be taken in consideration [44]. This results in a constant shift of the frequencies and to a shift of the different transversal modes. The new resonance frequencies are

$$\nu_{q,l,m} = q\nu_F + (l + m + 1) \frac{\Delta\xi}{\pi} \nu_F, \quad (3.24)$$

with the difference $\Delta\xi$ of the Gouy-phases at the mirrors.

Calculations for both the mode-separation and the mode-matching to our cavity can be found in appendix A

3.2.2. Pound-Drever-Hall technique

To stabilize the output frequency of a laser, an element is required which transforms frequency deviations of the laser into an electronic signal. The transmission and reflection coefficients (equations 3.13,3.14) are symmetric signals around the central resonance frequencies of the resonator. This signal can therefore not be used as feedback on the laser. However, the Pound-Drever-Hall technique offers a solution to overcome this problem [45, 46]. Figure 3.5 shows a sketch of a common setup for this method. With an EOM the phase of the light of a laser is modulated with a frequency which can be controlled by an oscillator. The modulated light is coupled into a resonator and a photo-diode measures the reflected power. A mixer then multiplies the signal of the photo-diode with the signal of the oscillator. The phases of both signals can be matched with a phase shifter. After passing a low-pass filter, the resulting signal can be fed back to the laser by a PID controller to lock the frequency of the laser onto a resonance of the cavity.

The basic idea of this method is quite simple and can be described by a simple model. Equation 3.25 mathematically describes the consequence of phase modulation of a light field by an EOM. Here ω_0 is the frequency of the laser and Ω the frequency of the oscillator.

$$\begin{aligned} E(t) &= E_0 \cdot e^{i(\omega_0 t + \beta \sin(\Omega t))} \\ &\approx E_0 \cdot e^{i\omega_0 t} \left[1 + \frac{\beta}{2} (e^{i\Omega t} - e^{-i\Omega t}) \right] \\ &= E_0 e^{i\omega_0 t} + \underbrace{E_0 \frac{\beta}{2} e^{i(\omega_0 + \Omega)t}}_{E_{\text{side}}} - \underbrace{E_0 \frac{\beta}{2} e^{i(\omega_0 - \Omega)t}}_{E_{\text{side}}} \end{aligned} \quad (3.25)$$

The result of this equation means, that there are three frequency components in the laser after phase modulation. A carrier with frequency ω and two sidebands with frequency $\omega_0 + \Omega$ and $\omega_0 - \Omega$, respectively. In principle, the same result can be obtained by modulating the

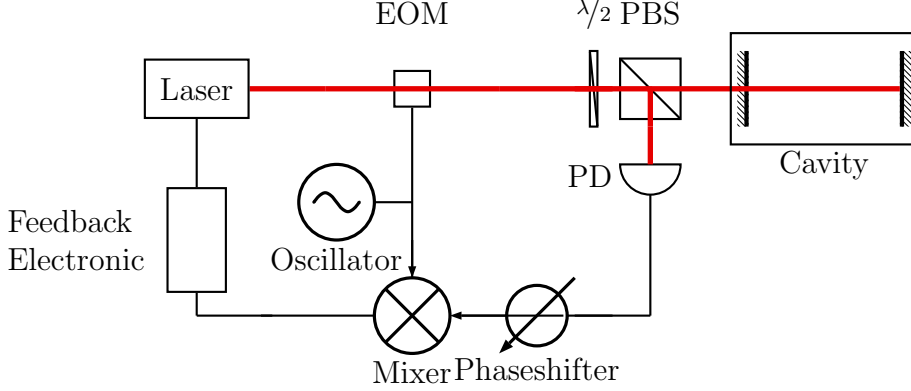


Figure 3.5.: Sketch of the setup for the Pound-Drever-Hall technique. An EOM is used to modulate sidebands onto the output of a laser beam. The beam is coupled into a cavity and the reflected signal is separated by a PBS and detected by a photo-diode. For the creation of an error signal the signal of the photo-diode is mixed with the modulation signal. Subsequently the error signal is fed into a feedback controller to stabilize the frequency of the laser.

current of the laser, but using an EOM offers the possibility to modulate only one single branch.

Thus the photo-diode in the setup detects the power of the light with these three frequency components. To calculate the resulting signal, we first have a look at the electric field of the reflected light.

The next step is to calculate the signal which is detected by the photo-diode. The combination of the phase modulation in equation 3.25 and the reflectance of the electric field (3.14) leads to

$$E_{\text{ref}} = \mathcal{R}(\omega_0)E_0e^{i\omega_0 t} + \mathcal{R}(\omega_0 + \Omega)E_{\text{side}}e^{i(\omega_0 + \Omega)t} - \mathcal{R}(\omega_0 - \Omega)E_{\text{side}}e^{i(\omega_0 - \Omega)t} \quad (3.26)$$

Correspondingly the power is

$$\begin{aligned} P_{\text{ref}} &= |E_{\text{ref}}|^2 \\ &= |\mathcal{R}(\omega_0)|^2 P_0 + |\mathcal{R}(\omega_0 + \Omega)|^2 P_s + |\mathcal{R}(\omega_0 - \Omega)|^2 P_s \\ &\quad + 2\sqrt{P_0 P_s} \text{Re}[\mathcal{R}^*(\omega_0)\mathcal{R}(\omega_0 + \Omega) - \mathcal{R}^*(\omega_0 - \Omega)\mathcal{R}(\omega_0)] \cos(\Omega t) \\ &\quad + 2\sqrt{P_0 P_s} \text{Im}[\mathcal{R}^*(\omega_0)\mathcal{R}(\omega_0 + \Omega) - \mathcal{R}^*(\omega_0 - \Omega)\mathcal{R}(\omega_0)] \sin(\Omega t) \\ &\quad + \text{terms oscillating with } 2\Omega t \end{aligned} \quad (3.27)$$

The different terms result from interference of different frequency components of the inci-

3. Rydberg excitation system

dent light. The constant terms result from interference of the single frequency components with each other, the terms oscillating with the modulation frequency Ω result from interference of the carrier with the sidebands and the ones oscillating with 2Ω are due to interference of the sidebands. The interesting terms are the one oscillating with Ω , because the sign of the prefactors is sensitive to the detuning of the laser frequency ω_0 to the resonance frequency of the cavity. This is exactly what is required as feedback signal for the stabilization of the laser frequency. However, for this purpose the prefactors have to be isolated from the oscillation. This is achieved by multiplying the signals of photo-diode and oscillator in a mixer and passing the resulting signal through a low-pass filter. From two mathematical identities ²³ it becomes clear, that multiplying two sine with the same frequency leads to a DC-signal and a signal oscillating with double frequency, while for the product of a sine and a cosine the DC-signal vanishes. Thus to ensure that two sine are multiplied a phase shifter is included in the circuit to compensate for phase shifts due to a delay between the signals. The low-pass filter finally separates the DC-signal and one obtains a signal like shown in figure 3.6.

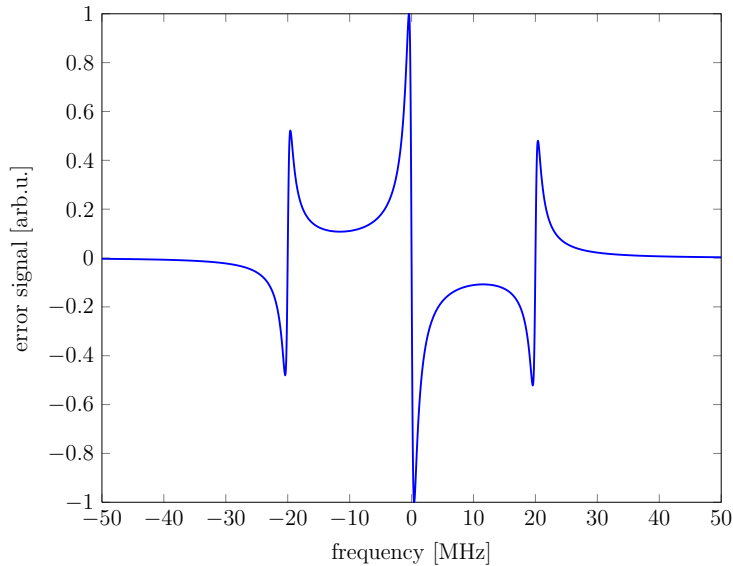


Figure 3.6.: Calculated error signal for a cavity with 1.5 GHz free spectral range, reflectivity of 99.8% and sidebands at ± 20 MHz. The steep slope around resonance is perfectly suited for frequency stabilization of a laser.

The signal shows a steep slope with a changing sign at the resonance and is therefore nicely suited as feedback on a laser.

² $\sin(a) \cdot \sin(b) = \frac{1}{2}[\cos(a - b) - \cos(a + b)]$,
³ $\cos(a) \cdot \cos(b) = \frac{1}{2}[\cos(a - b) + \cos(a + b)]$

3.3. Experimental setup

In this section the setup of the Rydberg excitation system is described. The section is divided into two parts, where the first part concentrates on the optical setup of the 480 nm and the 780 nm lasers as well as the setup of the reference cavity itself. In the second part the different electronic components which are necessary for the laser-lock are described.

3.3.1. Optical setup

The optical setup of the Rydberg excitation consists mainly of three parts. Two lasers operating at a wavelength of 480 nm and 780 nm, respectively, and the reference cavity.

Setup of the red 780 nm laser

In figure 3.7 a) the setup of the red 780 nm laser is shown. Here an extended cavity laser of the Toptica DLpro series with 60 mW of output power is used. Its output is divided into four branches by several beamsplitters for different purposes. The branch leaving the first polarizing beamsplitter (PBS) to the top side is used to determine the wavelength of the laser. The setup provides two methods with different resolution. First the output is coupled to a wavemeter, which allows the determination of the wavelength with an accuracy of 1 pm. Secondly the laser beam is overlapped with a beam of an additional laser which is locked to a Rubidium cell by DAVLL spectroscopy (see [26] for a description of the setup of this laser). The overlapped beams are focused onto a fast AC-coupled photodiode which is connected to a spectrum analyzer displaying the difference frequency of both lasers. For locking the laser to the reference cavity 2 mW of output power are coupled to a fiber-coupled EOM. To use the EOM efficiently, a $\lambda/2$ -waveplate is used in front of the fiber coupler to rotate the polarization of the laser parallel to the electric field of the EOM. The finally left branch is coupled to the fiber which is connected to the experiment. To switch the light on and off a mechanical shutter and an AOM are included in this path.

Setup of the blue 480 nm laser

For the second step of the Rydberg excitation a Toptica DLpro-TA-SHG system is used. Thereby a grating stabilized diode laser is used to create infrared laser light at a wavelength of 960 nm. A branch of this is split off and used for locking the laser to the cavity. The determination of the wavelength is done by a wavemeter and the third branch can be used for a measurement of the linewidth (compare section 3.4.3. The other branch is coupled into a tapered amplifier (TA) to increase the output power. The amplified infrared light is then coupled into a bow-tie cavity with one mirror adjustable by a piezoelectrical element. By current modulation of the laser diode sidebands are modulated onto the light. Therefore the optical path length of the cavity can be locked by a Pound-Drever-Hall lock to resonance with the laser light. This provides high electric field inside the cavity. With a nonlinear

3. Rydberg excitation system

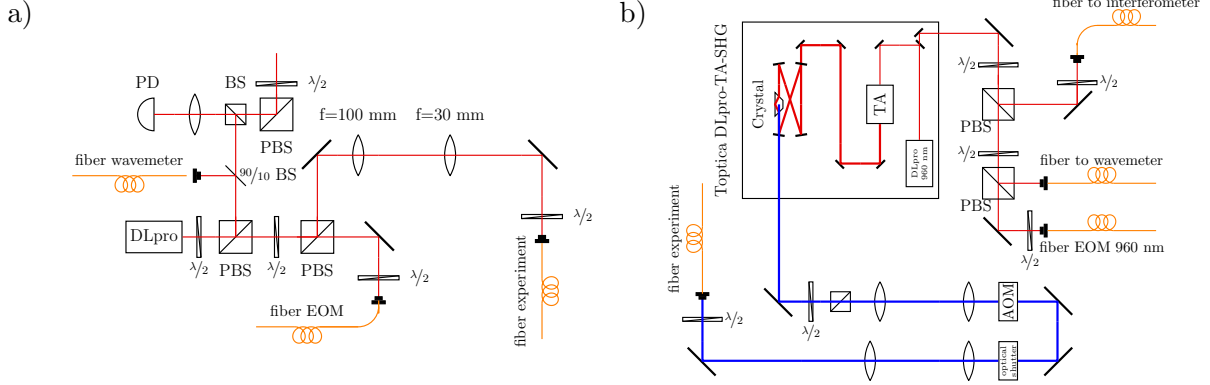


Figure 3.7.: Optical setup of the two Rydberg-lasers. For the excitation to the intermediate $5P_{3/2}$ -level a diode laser operating at 780 nm is used (a)). The second step to the Rydberg level is done by excitation with 480 nm light produced by a frequency-doubling system (b)).

crystal the electric field is used to create frequency-doubled laser light by second harmonic generation. With this system it is possible to create up to 400 mW of blue laser light at a wavelength of 480 nm.

The sidebands on the infrared light do not pose a problem for the Rydberg excitation, as these components are not resonant to the bow-tie cavity and therefore not frequency doubled. However the sidebands can be directly used to lock the infrared diode laser to the reference cavity.

For switching the light on and off at the experiment, in this setup also a mechanical shutter and an AOM are used. An optical fiber delivers a high-quality Gaussian mode to the experiment.

Setup of the reference cavity

Both Rydberg excitation lasers are stabilized to the same cavity. This is a passively stable resonator produced by Stable Laser Systems. Figure 3.8 shows a picture of the cavity. The crucial part of this cavity is a spacer on which the mirrors are mounted in a distance of 10 cm. This spacer is made from Ultra-Low Expansion (ULE) glass, a special kind of glass with excellent properties concerning the thermal expansion of the material. ULE glass has a zero crossing of the coefficient of linear thermal expansion at a critical temperature T_c around room temperature. Therefore one is left with a quadratic dependence of the thermal expansion coefficient at this temperature, which is given by ([47])

$$\frac{\Delta L}{L} = 10^{-9} \cdot (T - T_c)^2. \quad (3.28)$$

To reach a high thermal stability, the temperature of the cavity has to be stabilized around this temperature. For doing so, the ULE spacer is placed on a Zerodur-block which is placed

3. Rydberg excitation system

inside an aluminium vacuum can. This setup ensures that the ULE-spacer is thermally isolated from the environment. An ion-getter pump is connected to the aluminium can and provides a vacuum below 10^{-8} mbar. Thus radiation is the main mechanism for heat transport from the vacuum can to the inner parts. The temperature of the can is stabilized by thermo elements which are connected to a commercial temperature controller.

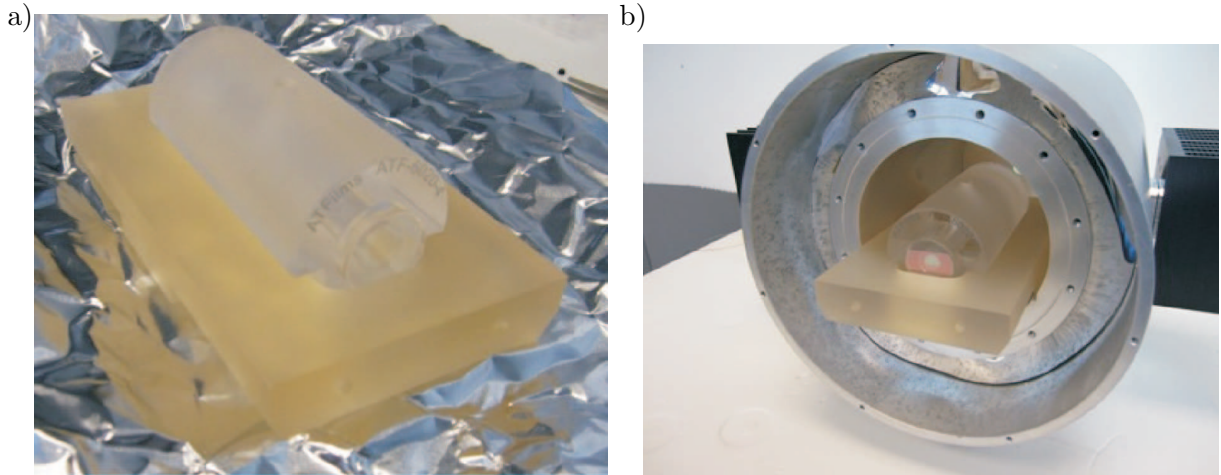


Figure 3.8.: Pictures of the assembly of the reference cavity. a) shows the ULE-block which is used as spacer between the mirrors, providing the high stability of the cavity. b) The ULE-spacer is placed on a Zerodur-block inside an aluminium vacuum can to thermally isolate it from the environment. The temperature inside the vacuum can is kept constant by peltier elements which are controlled by a temperature controller.

The cavity itself is of the planar-convex type consisting of a planar mirror and a second mirror with a curvature of 500 mm. These mirrors have a reflection coating for the wavelength of 780 nm and 960 nm leading to a Finesse of 1800 at both wavelengths. The calculation for the mode matching into the cavity can be found in the appendix A. Figure 3.9 shows a sketch of the optical setup used for the Pound-Drever-Hall lock. The laser beams, guided through optical fibers to the cavity, are each collimated by $f = 4$ mm lenses. For the mode matching we decided to use one further lens for both beams and to couple through the curved mirror. This has the advantage that the distance between cavity and lens is smaller than for the other case as the length of the cavity is included in the distance between lens and focal point and the curved mirror acts as a lens itself.

Both beams are overlapped with a PBS which also proves that the polarization of both beams are perpendicular to each other. As the beams reflected from the cavity have the same polarization as the incident beams the different wavelengths are separated by the PBS again. The intensity of the reflected beams is measured by the photo-diodes PD 2 and PD 3 respectively. These are amplified silicon photo-diodes with a bandwidth of 150 MHz ⁴.

⁴Thorlabs PDA10A-EC

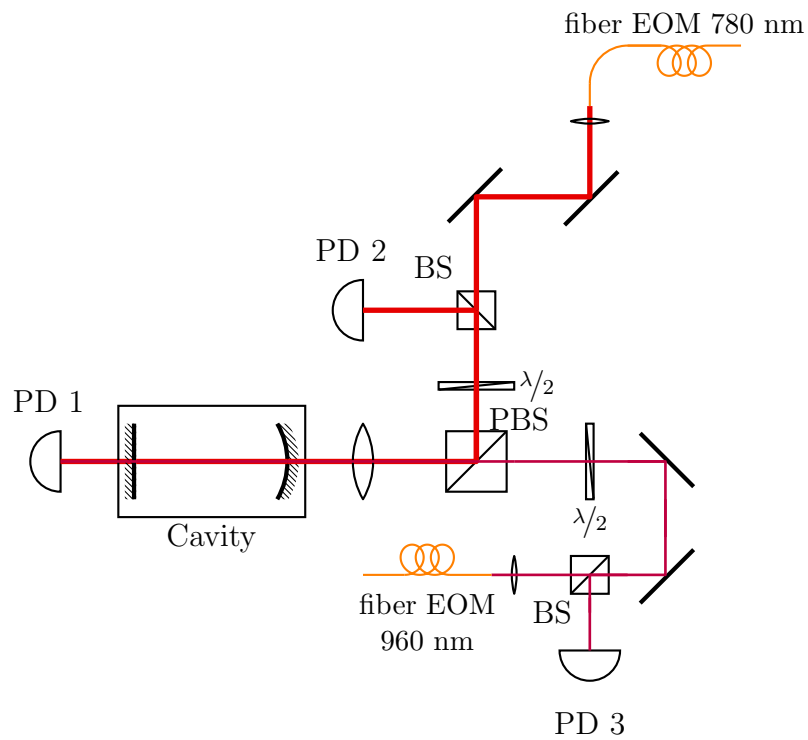


Figure 3.9.: Schematic drawing of the optical setup for stabilization the Rydberg lasers to the reference cavity. The light coming from the lasers through optical fibers is collimated with aspheric lenses and overlapped with a PBS. For mode-matching one single lens is used for both wavelengths. The intensity of the reflected beams is measured with the photodiodes PD 2 and PD 3 respectively. PD 1 can be used for both optimizing the coupling to the cavity and finding the right lock-point.

3.3.2. Electronic setup

For the operation and locking of the lasers, several electronic components are required. For obtaining the error signals we are using commercial Pound-Drever-Hall modules ⁵. These provide a modulation with a frequency of $\nu_{\text{PDH}} = 20$ MHz used to modulate the sidebands on the laser. For modulating the 780 nm we apply this signal to the fiber-coupled EOM, on the blue laser the sidebands are created by modulating the current of the laser diode. By connecting the photo-diodes measuring the reflected intensity to the same module the error signal is produced. For locking on the slope we use then a commercial high-bandwidth PID-controller ⁶. A more detailed description of this PID-controller can be found in section 3.4.2.

However, with these parts it is only possible to stabilize the laser to a certain frequency. Though, in a common Rydberg experiment the opportunity for scanning the frequency of the laser stepwise across the transition is required. Different approaches offer a realization. First, mounting one of the mirrors of the cavity on a piezo element allows to change the resonance frequency by varying the distance between the mirrors. Certainly, this method is limiting the long-time stability of cavity as the temperature stability of the piezo element is worse than the one of the ULE-spacer.

On the other hand, using an acousto-optical modulator (AOM) in the experiment branch of the laser allows changing the output frequency and simultaneously keeping the distance between the mirrors of the cavity fixed. This solution is, however, less flexible as an AOM can only cover a small frequency range of the free-spectral range. Passing one AOM several times increases this range, but also leads to a loss of laser power.

For this reason we implemented another solution in our setup. The fiber-coupled EOMs are used to modulate further sidebands with a variable frequency between 60 MHz and 700 MHz, referred to as frequency-offset ν_{fo} from now on. In the case of the 780 nm Rydberg-laser, both modulation signals are mixed in a power splitter and coupled to one single EOM. The phase modulation with frequencies ν_{PDH} and ν_{fo} results in a variety of sidebands. Demodulation of the reflected cavity signal with the Pound-Drever-Hall module results in three error signals, one at the position of the carrier frequency and two further shifted by $\pm\nu_{\text{fo}}$. Locking the laser on one of the sidebands created by this technique and simultaneously changing the frequency ν_{fo} changes the output frequency of the laser, as the feedback to the laser keeps the resonant to the cavity. Due to the feedback of the PID-controller the laser frequency is changed such that it remains resonant to the cavity. This scheme enables to change the frequency of the locked laser by nearly half the free-spectral range.

For not degrading the lock quality of the laser by using this technique, it is important that the frequency source used for modulating the sidebands has a narrow bandwidth and is not drifting with time. For this reason we use a self-built digital frequency synthesizer based on a DDS-chip (direct digital synthesis) developed by the faculty electronics workshop ⁷. Figure 3.10 shows a measurement of the output linewidth of the driver operated at 300 MHz.

⁵Toptica PDD 110

⁶Toptica FALC110

⁷ELAB 70/10

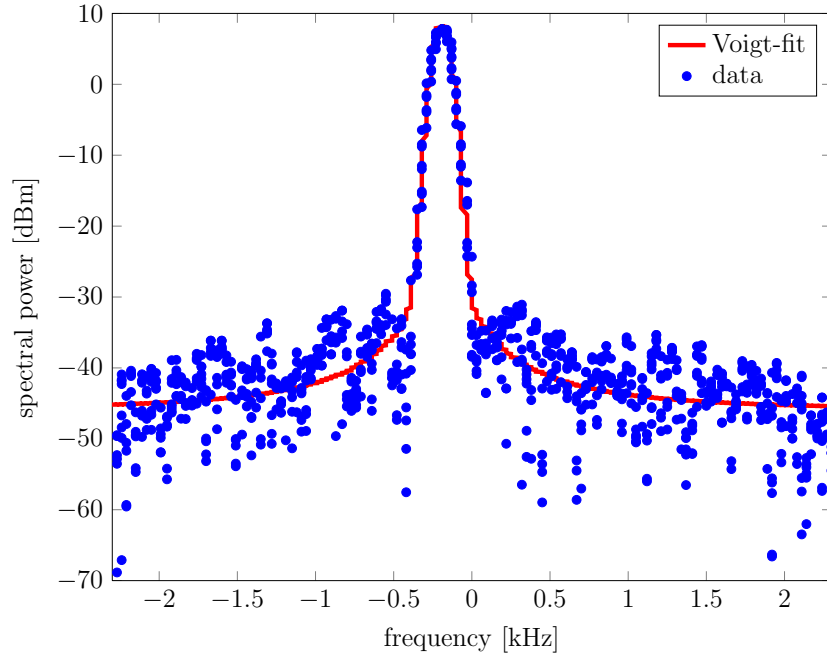


Figure 3.10.: Output spectrum of the digital frequency synthesizer ELAB 70/10 operated at a frequency of 300 MHz, for clarity the peak is shifted to zero. A Voigt-fit to the data points yields to a FWHM of 66 Hz. During one day, no shift of the resonance frequency was observable.

For clarity the peak was shifted to zero afterwards. A Voigt fit to data yields to a linewidth (FWHM) of 66 Hz. Concerning the long time stability no drift was observable on the timescale of one day. The frequency can be digitally set in the range between 3 MHz and 320 MHz. Up to 16 frequency synthesizers can be connected to a three-line bus system which is connected to the computer control system. Programming is done by the SPI (serial peripheral interface) protocol which is implemented in the computer control system. Additionally, the frequency can be changed stepwise by applying a signal with rising edge to a fourth input. This function can be used to scan the laser across atomic transition while it is locked.

However to cover the full free-spectral range, sidebands shifted up to 750 MHz are required. This problem is solved by using frequency doubling devices. A circuit diagram of the used components can be found in appendix B.

3.4. Characterization and optimization of the stability

In this section different experimentally measured properties of the Rydberg-laser system are described. A detailed characterization of the cavity and the created error signals is followed by an analysis of the laser electronics and the feedback loop. Subsequently different methods to determine the linewidth of the frequency stabilized laser system are introduced. Finally, the results obtained by Rydberg spectroscopy in the already existing setup are discussed.

3.4.1. Characterization of the resonator

In order to prove the coupling to the cavity a transmission spectrum of the laser was taken. In the measurement of figure 3.11 a) the transmission of the cavity for the 780 nm laser was recorded, while the frequency was scanned across the free spectral range by tuning the voltage of the piezo element. The spectrum shows six peaks of which the two tall ones can be assigned to the carrier frequency and the ones with a lower amplitude refer to the sidebands for the Pound-Drever-Hall technique. Width and position of the peaks were determined by fitting Lorentzians to the data. Figure 3.11 verifies the high accuracy of the fit. With the known frequency difference of 20 MHz between carriers and sidebands the x-axis was scaled in frequency units. This leads to a free spectral range, as the width between the carriers, of

$$\Delta\nu = 1.506 \text{ GHz} \pm 52 \text{ MHz},$$

which is in very good agreement with the theoretical value of 1500 MHz for the 10 cm long cavity. In combination with the width of the peaks of

$$\nu_{1/2} = 939 \text{ kHz} \pm 71 \text{ kHz}$$

the resulting finesse is

$$\mathcal{F} = 1603 \pm 177.$$

Besides the measurement shows nicely that the higher spatial modes are suppressed nicely, indicating that the mode matching and coupling to the cavity fits with high precision. However, to measure the distance between higher spatial modes the coupling was degraded. The related measurement is shown in figure 3.11 c). In this measurement the peaks labeled as zeroth order are the same as in the case for perfect coupling. The peaks appearing with lower amplitude belong to the next higher order of spatial modes. From the fit a spacing between the modes of $223 \text{ MHz} \pm 3 \text{ MHz}$ was measured according to the calculated value of 221 MHz calculated in appendix A.

Important for the stabilization of the lasers are the error signals obtained by the Pound-Drever-Hall method. These are shown in figure 3.12 a)-c) for the DLpro and in d)-f)

3. Rydberg excitation system

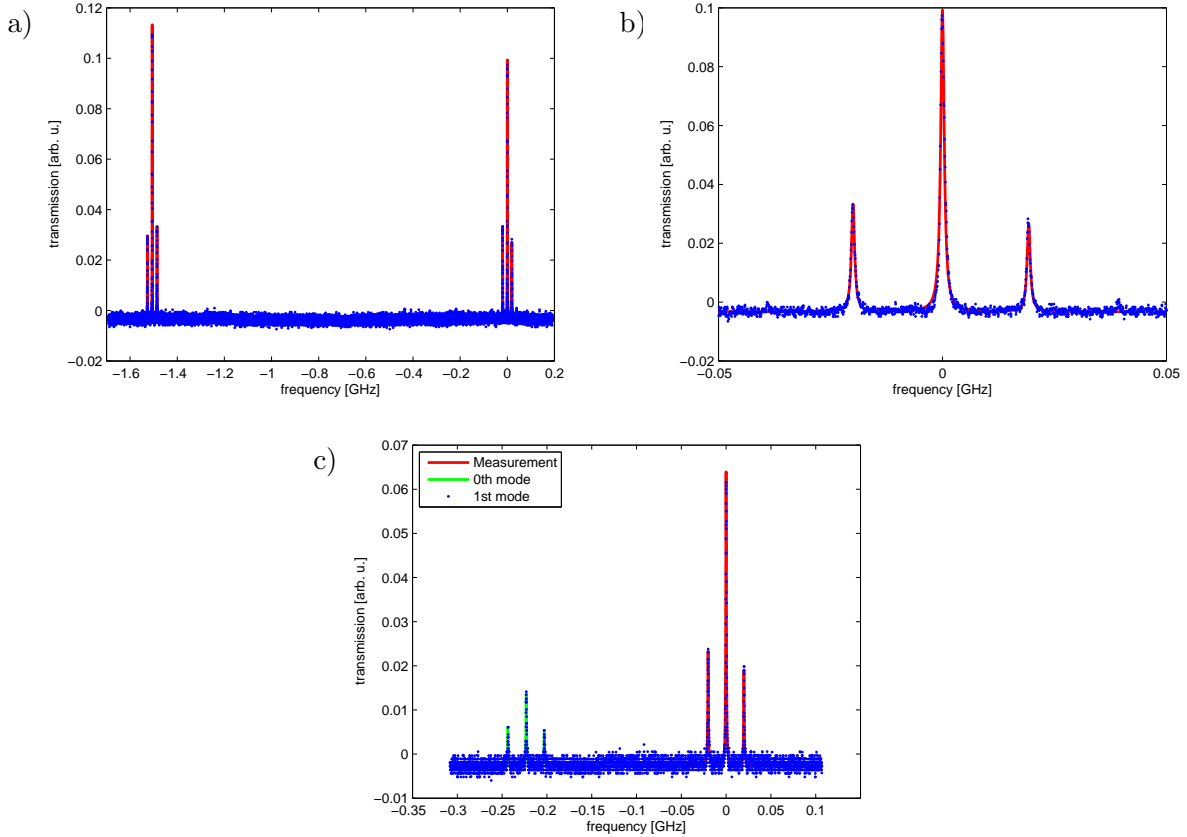


Figure 3.11.: Experimental transmission-spectrum through cavity. Scan across one single free spectral range a), resolved single transmission peak with the small sidebands b) and a higher spatial mode due to misalignment c).

for the TA-SHG. Each subplot shows three different error signals which have the shape expected from the calculations in section 3.2.2. The centered error signals belong to the carrier-frequency of the laser, the other two error signals symmetrically placed on the sides belong to the sidebands modulated with the frequency synthesizers. From top to bottom the frequency differences ν_{fo} between the centered and the outer error signals are 90 MHz, 300 MHz and 600 MHz for the DLpro and 90 MHz, 360 MHz and 600 MHz for the TA-SHG. The interesting quantities to be extracted from these signals are the amplitude and the signal per kHz deviation from the center frequency of the steep slope. The combination of these parameters defines the capture range of the error signal, which is the frequency span in which the laser can be stabilized by feedback.

The capture range was obtained from data by fitting a straight line to the slope of the error signals. With the result the x-axis was scaled by the known distance between the zero-crossings of the error signals. From the slope of the fit and the amplitude of the error signal the capture range could be determined. The resulting values are:

3. Rydberg excitation system

	DLpro	TA-SHG
ν_{fo}	capture range	
90 MHz	690 kHz \pm 78 kHz	557 kHz \pm 36 kHz
300 MHz	578 kHz \pm 22 kHz	-
360 MHz	-	592 kHz \pm 48kHz
600 MHz	570 kHz \pm 35 kHz	592 kHz \pm 45kHz

All values are the mean of the three error signals shown in each subplot, justified by the fact that the deviation among them is very small. The specified errors were calculated by error propagation from the errors obtained by the fit.

Within the error bars all results are equal except the 90 Mhz sidebands in the case of the DLpro. Having a closer look at this data the higher value is not astonishing as there is a lot of noise on the signal. This might be caused by the mixing of the two rf-signals in the power-splitter when the frequencies are too close to each other.

One can observe a change in the amplitude of the error signal when the laser offset frequency ν_{fo} is changed. This has a negative impact on the lock quality when the laser is scanned. The reason for this behavior is the frequency doubler used in the setup which has an output level that is not constant on the complete frequency range. A voltage controlled attenuator might be a solution to flatten the output level for the EOMs by applying suited voltage when the laser is scanned.

3. Rydberg excitation system

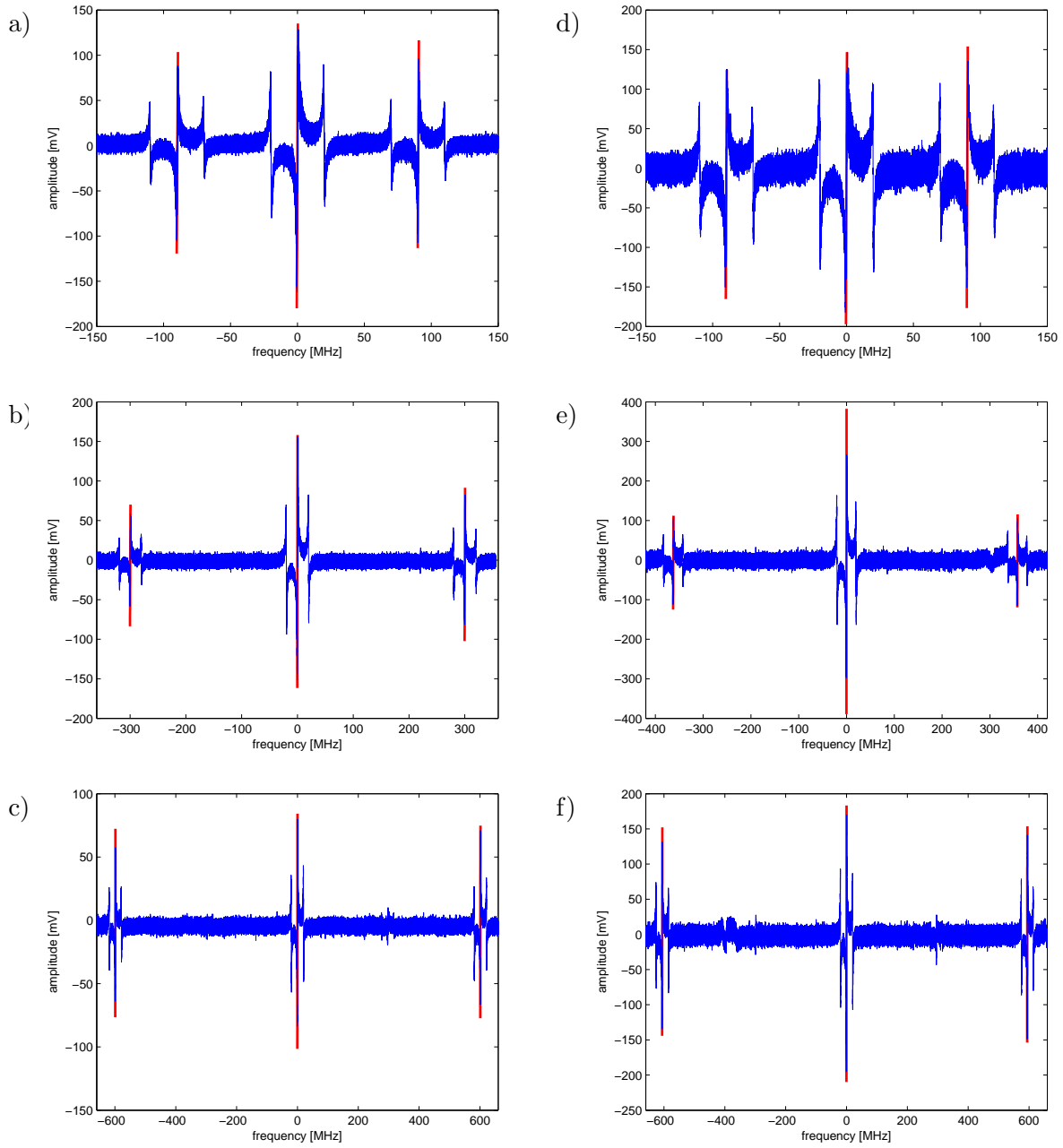


Figure 3.12.: Error signals of the DLpro a)-c) and the TA-SHG d)-f) obtained for different modulation frequencies ν_{f_0} .

3.4.2. Feedback loops

As already described earlier, the error-signal obtained by the Pound-Drever-Hall technique is fed back to the laser by a controlling device. The quality of such a feedback system can be investigated by means of control theory [48]. In the following a few basic properties of feedback systems are discussed.

The ultimate goal of control theory is to generate a system, which has an output that is following an input signal with high accuracy. For analyzing a circuit the transfer function $P(\omega)$ is, according to figure 3.13, defined as

$$s(\omega) = P(\omega)C(\omega), \quad (3.29)$$

where $s(\omega)$ is the output of a system modulated by $C(\omega)$. In principal, when the transfer function $P(\omega)$ is known, one could now apply the input which is required for a desired output $R(\omega)$. However, problems occur if the transfer function has resonances for certain modulation frequencies which are accompanied with a phase lag, or if there is noise on the input signal.

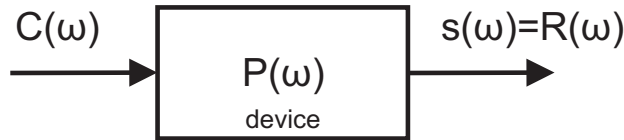


Figure 3.13.: Response function of an ideal system without noise

This situation is illustrated in figure 3.14. Due to the noise $n(\omega)$ the total input changes to $C(\omega) + n(\omega)$, leading to an output of the device $s(\omega) = P(\omega) \cdot (C(\omega) + n(\omega))$. This means that the actual output deviates from the desired output by $\epsilon(\omega) = s(\omega) - R(\omega) = P(\omega)n(\omega)$.

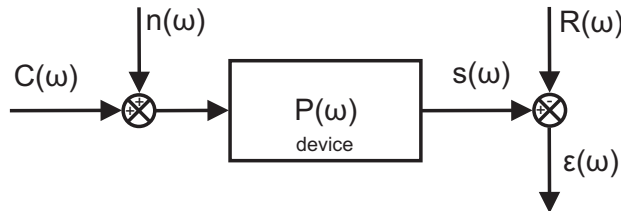


Figure 3.14.: Response function of a system with noise

To minimize this deviation feedback loops are used. Therefore the error $\epsilon(\omega)$ is applied to a controller with gain $H(\omega)$. Subsequently the output of the controller is subtracted from the input of the device like depicted in figure 3.15.

Taking this feedback into account the total output $s(\omega)$ of the device is

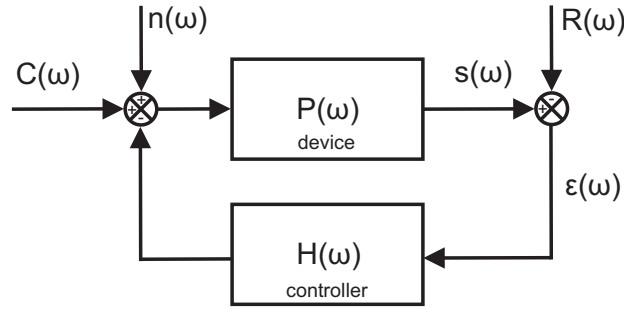


Figure 3.15.: Feedback loop to minimize noise

$$\begin{aligned}
 s(\omega) &= P(\omega) \cdot (C(\omega) + n(\omega) - H(\omega)\epsilon(\omega)) \\
 s(\omega) &= R(\omega) + P(\omega)n(\omega) - P(\omega)H(\omega)\epsilon(\omega) \\
 (1 + P(\omega)H(\omega))\epsilon(\omega) &= P(\omega)n(\omega) \\
 \epsilon(\omega) &= \frac{P(\omega)n(\omega)}{1 + P(\omega)H(\omega)}. \tag{3.30}
 \end{aligned}$$

Thus, the error $\epsilon(\omega)$ is reduced by a factor $\frac{1}{1+P(\omega)H(\omega)}$ in contrast to a system without feedback. One defines the open loop gain $G(\omega) = P(\omega)H(\omega)$ and the closed loop gain $G_c(\omega) = \frac{1}{1+G(\omega)}$. It is important to remark that the gain $G(\omega)$ is a complex quantity, consisting both of an amplitude $|G(\omega)|$ and a phase $\varphi(\omega)$, connected by $G(\omega) = |G(\omega)|e^{i\varphi(\omega)}$. Problems occur when the phase reaches 180° and the amplitude has a finite value. In this case noise is amplified instead of canceled out.

For the choice of the feedback-controller it is very common to use a PID-controller, which is composed of three parts, a proportional part (P), an integral part (I) and a derivative part (D). In frequency domain the output $K(\omega)$ of a PID is of the form

$$K(\omega) = K_p + \frac{K_i}{i\omega} + iK_d\omega. \tag{3.31}$$

The frequency dependent behavior of the different parts are shown in figure 3.16 a)-c), where frequency response of amplitude and phase are illustrated in Bode plots. The response of the P-part is always proportional to the error which is applied to the controller and the signal is in phase with the modulation. This behavior is fine to cancel out small drifts. However, the fact that the gain stays constant for high frequencies causes problems when the phase of the feedback loop reaches a value of above 90° . In this case the noise is even amplified and the system is no more stable. The integral part offers the possibility to raise the gain of the controller for small frequencies, as it sums up the error for a certain time. It is important to remark that the feedback of the integral part suffers a phase shift of -90° . Finally the derivative part can be used to raise the gain and in particular the phase for high frequencies and thus helps to raise the regulation bandwidth compared to a PI-loop

3. Rydberg excitation system

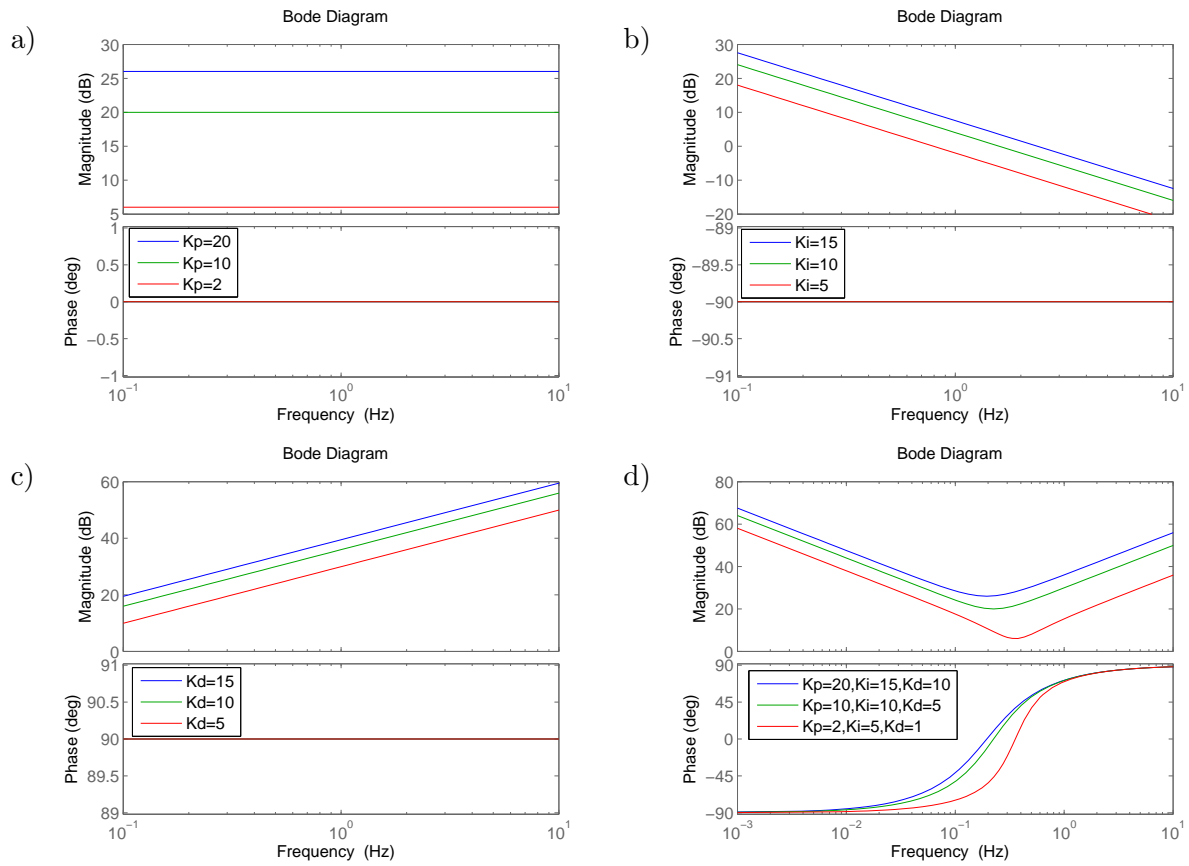


Figure 3.16.: Bode plots of proportional-part (a)), integral-part (b)), derivative part (c)) and assembled PID controller for different values. The parameters were chosen arbitrarily.

only.

Characterization of the laser electronics

Before the PID-controller was optimized to our system, the transfer functions of several components in the feedback loop were measured. This was done by applying a sinusoidal voltage to the device with a computer controlled function generator ⁸. With a computer controlled oscilloscope ⁹ both the applied signal and the response signal of the device were recorded. A software extracts the phase between the two signals and the amplitude of the response signal. Figure 3.17 shows the results for the scan controller ¹⁰ a), the piezo b), the current controller ¹¹ c) and the laser diode d).

In the setup the scan controller is used to control and modulate the voltage of the piezo element which is used to change the wavelength of the laser by changing the position of the grating. This controller has an external voltage input which can be used to change the high voltage output. For the data in fig 3.17 a) phase and amplitude of these two signals were compared to each other. The Bode plot shows that both amplitude and phase break down at a modulation frequency of 50 kHz.

The transfer function of the piezo element itself cannot be obtained that easily. It is not possible to modulate the piezo element by applying the voltage of the function generator, instead the modulation is applied to the scan controller. Thus the obtained transfer function describes the transfer function of the composed system and not of the piezo element itself. Moreover there is no possibility to measure the impact of the modulation on the piezo element directly. Hence a Rubidium cell was placed in the laser beam and the laser frequency was set to the slope of Doppler broadened absorption dip. A photo-diode behind the cell can then be used to transfer modulations of the laser frequency into a voltage modulation which can be detected by the oscilloscope.

Figure 3.17 b) shows the transfer function of these components. Here the phase reaches the critical value of 90° at a frequency of 3 kHz. This wouldn't be a problem if the gain is low at above this frequency, but the measurement shows that there are several resonances with higher gain above the critical frequency for the phase. These resonances are caused by the system consisting of piezo and grating which acts like a driven harmonic oscillator.

The important conclusion of the transfer function of the piezo is that the modulation of the feedback loop should be cut off for the piezo element above 3 kHz. Otherwise the system will run into instability as an error will be increased then.

In figure 3.17 c) the transfer function of the current controller which provides the laser diode with a constant current is shown. For this measurement a resistor was connected to the output of the current controller for being able to tap a voltage. A value of 10 Ω was chosen for the resistor as this is the typical resistance of a laser diode. Thus, a change of current supplied by the controller transfers linearly to the measured voltage. For this

⁸Velleman PCS500

⁹Velleman K8016

¹⁰Toptica SC110

¹¹Toptica DCC110

3. Rydberg excitation system

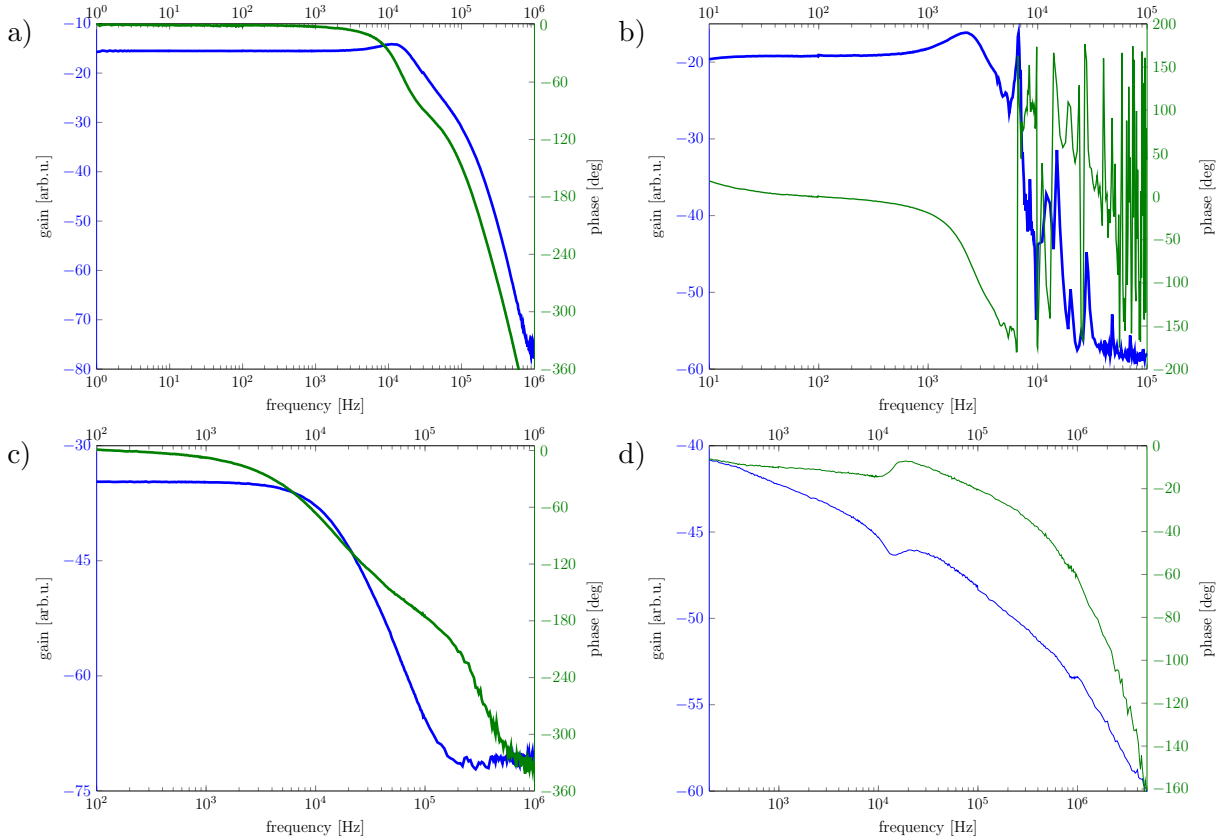


Figure 3.17.: Measured transfer functions of the Laser electronics. The transfer functions belong to a) scan controller Toptica SC110, b) piezo, c) current controller Toptica DCC110 and d) laser-diode.

controller the phase reaches 90° at a frequency of 10 kHz.

By modulating the frequency via an additional modulation input yields a better result. The principle of this modulation input is based on a MOSFET permanently sidelining some of the current provided by the current controller. As the amount of sidelined current depends on the voltage applied to the gate-input of the MOSFET, this schemes provides a mean to modulate the current of the laser diode with a high bandwidth.

Figure 3.17 d) shows the response function of the laser using this input. For converting the frequency changes caused by the current modulation into a voltage signal, the technique using the rubidium cell was applied again. The result shows that the laser diode can be modulated with a frequencies up to 2 MHz . At this frequency the phase reaches the critical value of 90° .

Additionally, the a resonance in gain at approximately 20 kHz can be observed accompanied by a small phase jump. The reason for this behavior are so called relaxation oscillations [49]. Changing the current of the laser diode leads to a change of the rates of stimulated emission and the pump rate to the excited level. These rates are coupled to each other and undergo damped oscillations until the reach a equilibrium level when the current is

3. Rydberg excitation system

changed. Resonance occurs when the modulation frequency of the laser current and the frequency of the relaxation oscillations coincide with each other.

As the modulation bandwidth of the laser diode itself is about two orders of magnitude higher than the modulation bandwidth of the current controller, the method of choice is to modulate the laser diode directly in the feedback loop and not to use the current controller.

Characterization of the feedback-loop

To close the feedback loop we use the commercial PID-controller FALC110 from Toptica. Figure 3.18 shows the principle of this device with a high bandwidth.

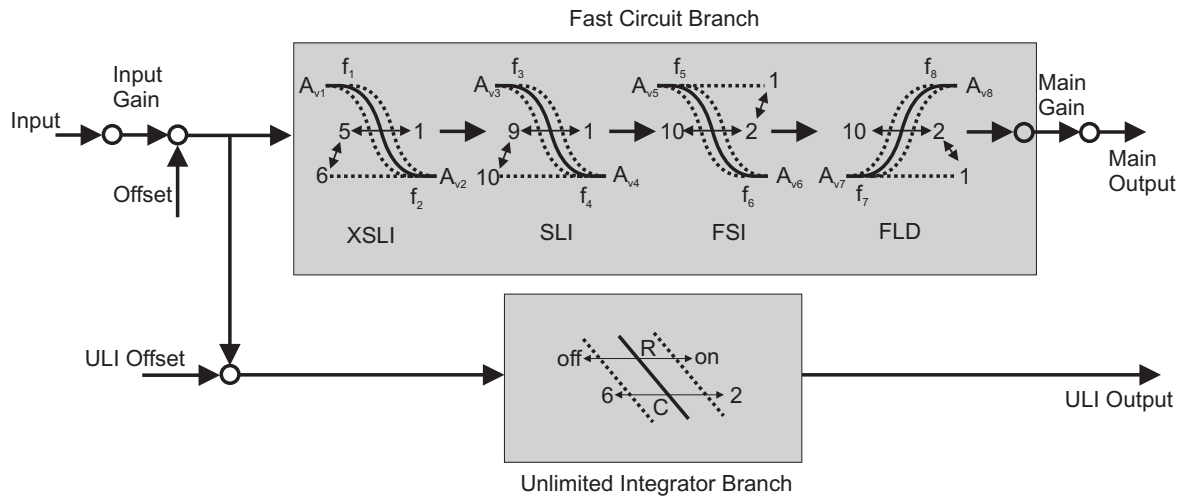


Figure 3.18.: Schematic drawing of the electronic structure of the FALC [according to the manual]. The feedback-loop is split into a fast and a slow branch.

After the error signal is added to the controller two trim-pots can be used to adjust both the amplitude by a gain factor between 1 and 10 and the offset. After this stage the signal is split into two amplifier branches with different bandwidth.

The first exists of three limited integrators and one limited differentiator in a row. Limited means that the gain of these elements is restricted to a certain value and does not reach zero or infinity. While the gain levels are fixed from the company the corner frequencies (denoted by the horizontal arrows in figure 3.18) of the different stages can be adjusted by several dip switches on the front panel of the controller.

With this design one can raise the gain of the controller stepwise by the three integrators for lower frequencies. Due to the limitation of the integrators one can ensure that the gain is not too high for high frequencies and raise it for lower frequencies only. The limited differentiator on the other hand offers the opportunity to reduce phase shifts of the control circuit occurring at high frequencies. Thus one can win further bandwidth.

The second branch consists of one unlimited integrator. There are also several dip switches which can be used to set the slew-rate of the integrator to a certain value. This branch is important for the low frequencies of the laser as its gain reaches very high values then.

The benefit which is obtained by the design of this PID-controller is that one can use the two branches as feedback for the piezo and the laser-diode. With the knowledge of section 3.4.2 it is obvious to use the fast branch as feedback to the laser diode and the unlimited branch as feedback for the piezo element. With this solution it is guaranteed that the piezo element compensates for slow drifts of the laser frequency, while fast deviations are settled by adjusting the current of the laser diode.

3. Rydberg excitation system

An initial setting of the dip switches resulting in stable locking of the laser was found by systematically testing different settings with the goal of minimizing the error signal peak-to-peak amplitude.

Having found these settings the closed loop transfer function of the feedback loop was measured. To do this the output of the frequency generator described before was connected to a second input of the PID controller. The response of the system to this modulation was measured by connecting the oscilloscope to the monitor output of the error signal. The result is shown in figure 3.19 for both the DLpro and the TA-SHG.

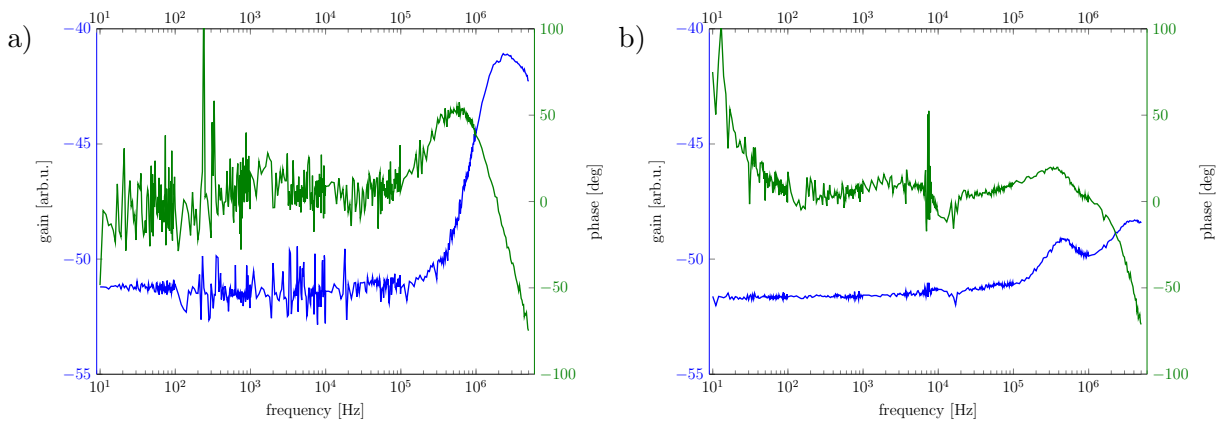


Figure 3.19.: Transferfunction of the closed loop for DLpro a) and TA-SHG b).

For frequencies up to more than 100 kHz no impact of the modulation on the error signal was visible. The gain which is measured in this region is completely dominated by the noise on the error signal. Therefore the value obtained for the phase is also not very reasonable in this regime as there is not really a relation between applied modulation and measured signal. Resulting from this fact strong oscillations in the phase are visible. Above 100 kHz a rise in gain occurs, which is in accordance with the observation of a modulation on the error signal in this frequency range. The phase finally drops below 45° for frequencies higher than 2 MHz. The measurement of the closed-loop transfer function of the TA-SHG feedback loop suffered from the same problems. Until 200 kHz the gain level remains flat and rises only little with increasing frequency. The phase buckles down at about 2 MHz, comparable to the measurement for the DLpro.

Unfortunately, the tools used for this measurement do not allow to measure frequencies above 5 MHz, but the frequency span which is of interest goes up to more than 10 MHz, defined by the bandwidth of the PID-controller. Additionally, to quantify the quality of the lock it would be important to measure the transfer function of the system without feedback. However, this is impossible as the laser therefore has to run stable on the slope of the error signal during the measurement.

To obtain better results it is essential to use a spectrum analyzer with high accuracy. For

3. Rydberg excitation system

measuring the feedback of both locked and free-running laser using a Rubidium cell could provide a suitable tool.

3.4.3. Measurement of the laser linewidth

Although section 3.4.2 gives a result for the bandwidth with which the laser system is stabilized, it gives no hint to the linewidth of the laser. Thus, other methods have to be used to answer this question. As the common tools for spectroscopy, like grating spectrometers or fabry-perot interferometers, have a resolution of about 10 MHz to 100 MHz they are not suitable for this purpose.

A more applicable solution is to use heterodyne detection methods. These are based on the detection of a wave by mixing it with another wave which is near resonant. There are in principal two slightly different approaches for such a linewidth measurement which will be described in this section.

Heterodyne linewidth measurement by a beatnote with a second laser

In section 3.2 the finite linewidth of a laser was explained by the fluctuations in the phase of the electric field. However it is impossible to measure these phase fluctuations. The purpose of heterodyne detection is to convert the phase fluctuations into intensity fluctuations.

The setup for the heterodyne linewidth measurement is quite simple and already illustrated in figure 3.7. A branch of the 780 nm Rydberg laser is overlapped with a second laser running at nearly the same frequency. In our case we use one of our MOT lasers which is stabilized to a Rubidium spectroscopy cell [26]. In order to get this technique for linewidth measurement working, it is important that the overlapping beams have identical polarization. With a fast AC-coupled photodiode the signal of the overlapped beams is detected and visualized by a spectrum analyzer.

For the interpretation of the results some theoretical description [50, 51] is necessary which will be shortly introduced here.

The signal measured by the photodiode is proportional to the incident intensity, this leads to a signal

$$I(t) = (E_1(t) + E_2(t))^2 = E_1(t)^2 + E_2(t)^2 + 2E_1(t)E_2(t), \quad (3.32)$$

where $E_{1/2} = \text{Re}(E(t)e^{i(\omega_{1/2}t + \phi_{1/2}(t))})$ is the electric field of laser 1 and 2, respectively. Hereby the first two terms represent the constant intensity of the components $I_{1/2}$, while the time-dependant third term represents the intensity $I_x = 2E_1(t)E_2(t)$ resulting from the mixing of the components. The constant signals are filtered out by the AC-coupled photodiode, so only the mixing component $I_x(t)$ survives.

The power spectral density which is detected with a spectrum analyzer can be calculated with the help of the Wiener-Kintchin theorem [52]. It states that the power spectral density S of a process is the Fourier transform \mathcal{F} of its autocorrelation G . Putting this together leads to

$$S_I(\omega) = \mathcal{F} \underbrace{\langle I_x(t)I_x(t + \tau) \rangle}_{G_I(\tau)}. \quad (3.33)$$

3. Rydberg excitation system

We can simplify this equation by expressing $I_x(t)$ by its relation to the electric field, leading to

$$\begin{aligned}
 S_I(\omega) &= 4\mathcal{F}\langle E_1(t)E_2(t)E_1(t+\tau)E_2(t+\tau)\rangle \\
 &= 4\mathcal{F}\langle E_1(t)E_1(t+\tau)E_2(t)E_2(t+\tau)\rangle \\
 &= 4\mathcal{F}(\langle E_1(t)E_1(t+\tau)\rangle\langle E_2(t)E_2(t+\tau)\rangle) \\
 &= 4\mathcal{F}(G_{E_1}(\tau)G_{E_2}(\tau)) \\
 &= (S_{E_1} \otimes S_{E_2})(\omega)
 \end{aligned} \tag{3.34}$$

From the second to the third line we made use of the mathematical fact that the mean of the product of two uncorrelated processes is equal to the product of their mean values. In the last step the convolution theorem was applied. So, the power spectral density of the heterodyne detection is equal to a convolution of the power spectral densities of the electric fields of both lasers. A calculation of the latter one can be found in [51].

This means that the width of the signal on the spectrum analyzer is always limited by the laser with the greater linewidth. For the determination of the linewidth of a laser it is necessarily required that the other laser has a much smaller linewidth.

Figure 3.20 shows two spectra with different resolution obtained by a Hameg HMS3000 spectrum analyzer with a sweeptime of 700 ms.

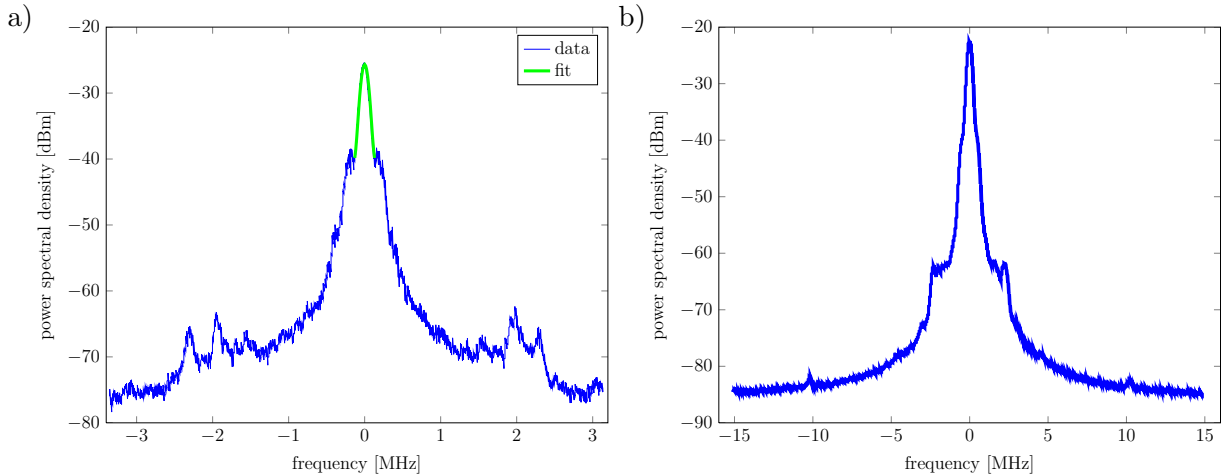


Figure 3.20.: Power spectral density of the beat signal between 780 nm Rydberg-laser and MOT-laser measured with different resolution. Besides the central peak with a width of 40 kHz additional sidebands at 200 kHz resulting from the feedback to the MOT-laser, at 2 MHz and at 10.5 MHz are visible.

The spectra show a narrow peak with a FWHM of 40 kHz, obtained by fitting a Gaussian to the center of the peak. Besides there are further sidebands symmetrically placed around the center.

The ones at 11 MHz, already damped by 60 dBm in contrast to the central peaks, can be further decreased by adjusting the gain of the PID-controller. In literature these peaks are

referred to as servo-bumps [53]. Their origin is the finite bandwidth of the feedback-loop. The distance of 11 MHz to the central peak fits well to the bandwidth specified for the PID-controller.

The other sideband cannot be affected by changing the settings of the lock of the Rydberg-laser. In [26] the ones at ± 200 kHz, damped by 15 dBm are related to the slower feedback electronics for the MOT-laser. They are therefore an artifact of the measurement and not present on the output of the Rydberg-laser.

Finally the sideband at ± 2 MHz, suppressed by 40 dBm, are still present when both lasers are unlocked. Their origin is an intrinsic effect of external cavity diode lasers [47]. They can be weakened by fast feedback to the laser diode but not completely suppressed. Also here we suffer from the slower feedback of the MOT-laser and cannot measure if these sidebands are damped in contrast to the free-running laser.

In the future a second Rydberg-laser operating at the same wavelength will give a tool to examine the stability in more detail.

Measurement of the long-time stability

To measure the long-time stability of the laser, the center-frequency of the measurement shown in figure 3.20 was red out for a time of 24 hours. The obtained data is plotted in figure 3.21.

It shows oscillations with a maximum amplitude of about 600 kHz and a cycle duration of approximately one hour. The frequency of these oscillations correlates with the drift of the stabilized temperature in the laboratory during the measurement. As the cavity itself is shielded from environment (3.3.1) one would not expect such correlations between a change of the temperature and a drift in the resonance frequency.

The drift is instead caused by the DAVLL-spectroscopy used to lock the second involved laser to a Rubidium-cell which is not temperature stabilized. The magnitude of the drift is also well in accordance with the data obtained from accurate observations on the temperature stability of DAVLL-spectroscopy [54].

Linewidth measured by a delayed self-heterodyne interferometer

The principle of the delayed self-heterodyne interferometer (DSHI) is the same as for a heterodyne linewidth measurement with a second laser. The difference is that only light of the laser which has to be characterized is used. Its output is split into two branches of which one passes an AOM and is shifted by a certain frequency, while the other one is delayed by passing an optical fiber. Afterwards both beams are overlapped again and detected by a fast photodiode. This procedure is necessary when using only one laser. Shifting the frequency of one branch prevents suffering from the strong intensity at zero and the delay actually offers the possibility to determine the linewidth.

In the limit that the delay-time τ_d is larger than the coherence time of the laser τ_c the the-

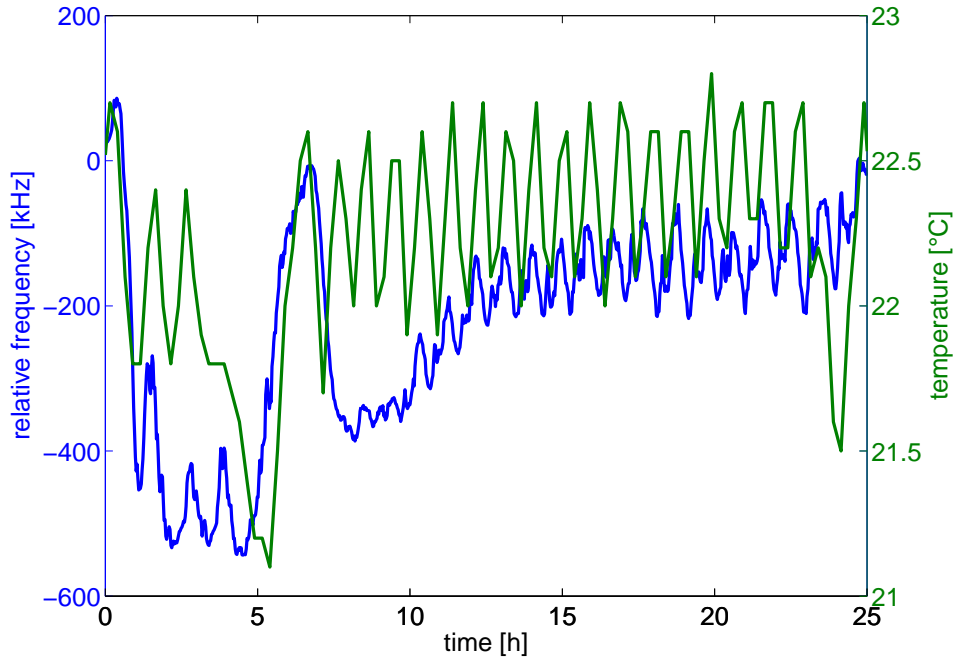


Figure 3.21.: Trace of the beatnote center frequency during 24 hours. The oscillations with a maximum amplitude of about 600 kHz are correlated to the temperature changes in the laboratory.

ory is the same as for a heterodyne detection with two lasers. In this limit the two beams are fully uncorrelated from each other and can be treated like two independent lasers.

When the delay time of the interferometer is in the order of the coherence time or even lower, the calculations of 3.4.3 for the power spectral density are not valid anymore, as both branches remain correlated. Nevertheless, assuming only white phase noise, it is possible to calculate an analytical solution in this case [55]. The resulting power spectral density has the shape of a Lorentzian with a δ -function sitting on the top. On the wings of the Lorentzian one can find oscillations with a frequency equal to the inverse of τ_d . The amplitude of these oscillations increases with decreasing ratio τ_d/τ_c .

In the case of $1/f$ phase noise no analytical solution for the power spectral density can be found. However, it can be shown that these components of the phase noise are filtered out for short delay times as the DSHI acts like a high-pass filter. For long delay times on the other hand, $1/f$ noise becomes more dominant in the spectrum.

For the measurement we used a setup already existing in our institute, illustrated in figure 3.22. In this setup a fiber with a length of 10524 m is used, leading to a delay time of $\tau_d = 52 \mu\text{s}$. With this delay linewidths down to 19.2 kHz can be measured.

Figure 3.23 shows the experimental results for DLpro and TA-SHG both locked and unlocked, respectively.

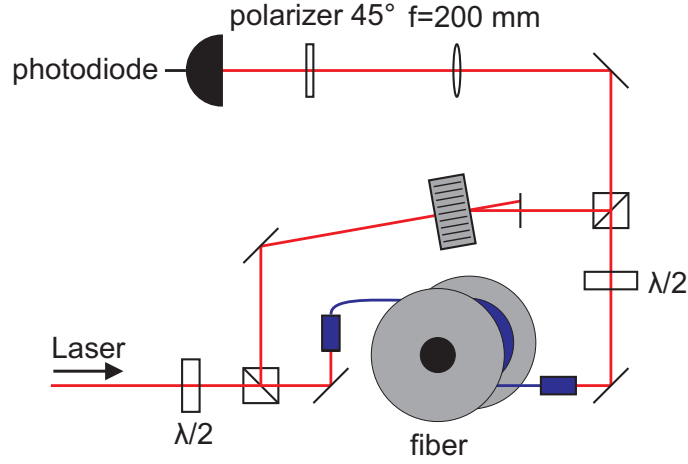


Figure 3.22.: Setup of the delayed self-heterodyne interferometer (taken from [51]). The beam of a laser is divided into two parts of which one is coupled into a 10 km long fiber, while the frequency of the other one is frequency shifted 80 MHz apart by an AOM. Both beams are overlapped again afterwards and detected by a fast photodiode

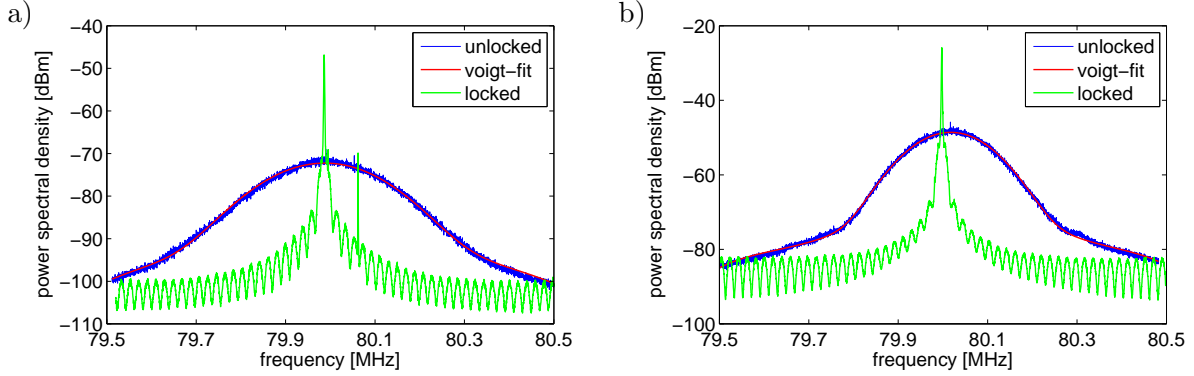


Figure 3.23.: Results of the delayed self heterodyne measurement for DLpro a) and TA-SHG b). Voigt-fits to the spectra of the unlocked lasers yield a linewidth of 157.4 kHz and 106.2 kHz for the free running DLpro and TA-SHG, respectively. The measurements for the locked lasers are below the resolution limit of 20 kHz.

In both cases the signal of the unlocked laser has the shape of a Voigt-curve. Numerical fitting to the data yields a width of

$$\Delta\nu_{\text{DLpro, unlocked}} = 157.4 \text{ kHz}$$

3. Rydberg excitation system

for the free running DLpro, and

$$\Delta\nu_{\text{TA-SHG, unlocked}} = 106.2 \text{ kHz}$$

for the unlocked TA-SHG. These values are within the limits of 100 kHz specified by the manufacturer on a timescale of 5 μs .

For the locked lasers the signal becomes much smaller compared to the signal of the free running laser. Moreover it shows the oscillating wings discussed above indicating a coherence time longer than the delay time. Trying to fit the function for the power spectral density for white phase noise from [55] to determine the linewidth failed. Therefore only an upper limit of 20 kHz can be given.

Noticeable in the signal of the locked DLpro is the additional peak on the right of the maximum. This peak does not result from the measurement and is therefore not a second dominant frequency of the laser. The reason for the peak are the long wires which were used to broadcast the signals from the interferometer to the laboratory with the lasers. These act like antennas and also receive rf-signals from the environment. This additional peak vanished by using shorter cables, which is the reason why it can not be observed in the signal of the TA-SHG.

3.4.4. Rydberg-spectroscopy in the existing setup for Rydberg experiments

As the setup of the new Rydberg apparatus described in section 2 does not provide the opportunity to take Rydberg-spectra yet, this was done in the already existing setup in the laboratory one floor below. Therefore, light from the new laser was coupled to the existing experiment via 20 m optical fibers. At this point only a short description of the used chamber will be given, further information is provided by [20], [56].

A rough illustration of experimental setup and sequence is shown in figure 3.24.

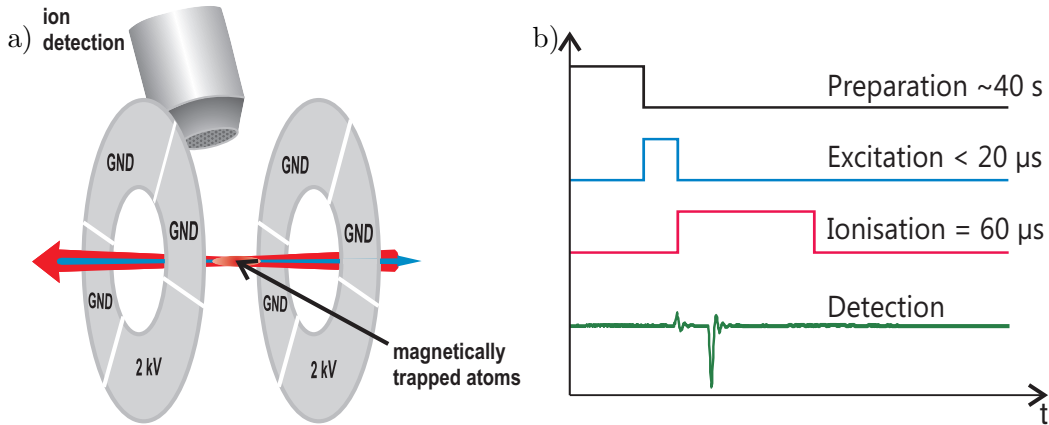


Figure 3.24.: Setup a) and sequence b) of the experiment used to measure the Rydberg spectra.

After trapping in a magneto-optical trap, the atoms are loaded into a magnetic trap where they are further cooled and optically pumped into the $|5S_{1/2}, F = 2, m_F = 2\rangle$ -state. After a preparation time of about 40 s densities of approximately $10^{12} \frac{1}{\text{cm}^3}$ are reached at a temperature of $1 \mu\text{K}$.

After applying a magnetic offset field of 13.5 G to split the magnetic sub-levels Rydberg atoms are excited. Therefore the red beam is aligned along the axis defined by the magnetic field, the blue laser exactly in the opposite direction. The frequencies of the lasers are set to two-photon resonance with the desired Rydberg-state. By choosing the polarization of the light, the desired magnetic sub-level can be addressed.

For the detection of the Rydberg atoms eight electric field plates are housed inside the vacuum chamber. Ramping them up to a high voltage after excitation ionizes the Rydberg atoms (see 4.1.2). Subsequently the ions are detected by a multi-channel plate. During one experiment cycle up to 400 excitation and detection processes can take place. The laser frequency is thereby changed in steps from shot to shot for scanning across the allowed transitions.

Spectroscopy on the 44D-state

Initially we started with spectroscopy on the $44D_{5/2}$ -state. The laser frequencies and polarizations were set according to the scheme illustrated in appendix C. By choosing σ^+ polarization of the lasers according to the preferred orientation of the spins defined by the magnetic field, the $m_j = 5/2$ -level is selected as single dipole allowed transition.

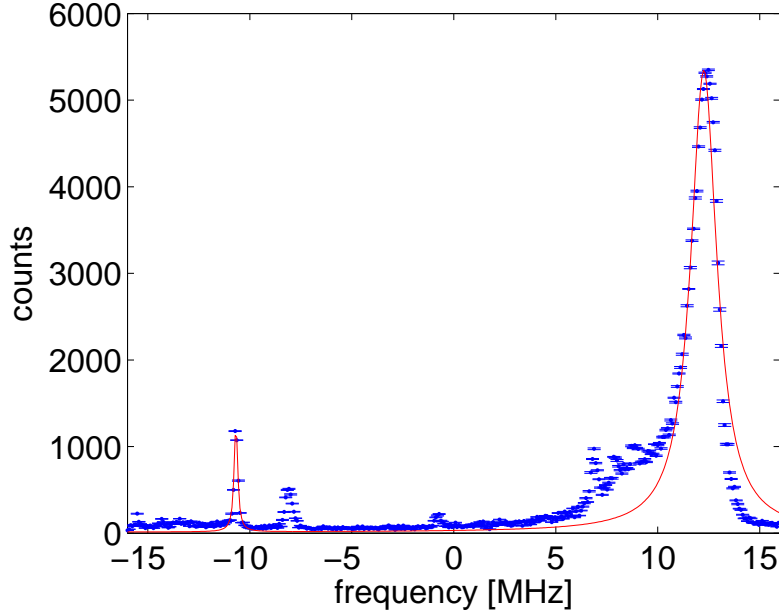


Figure 3.25.: Rydberg spectrum for the $44D_{5/2}$ -state.

Figure 3.25 shows the first Rydberg-spectrum obtained with the new laser system by a scanning across resonance with a span of 30 MHz. The spectrum shows several peaks at different positions. With a fit the frequency difference between the left and the right peak could be determined to be 22.93 MHz. This corresponds to the Zeeman-shift of the magnetic sub-levels of the $44D_{5/2}$ Rydberg state for a magnetic field of 13.65 G. Therefore the large peak corresponds to the $44D_{5/2}, m_j = 5/2$ -state and the small one on the right to the $44D_{5/2}, m_j = 3/2$ -state. Due to the transition rules the excitation to the $m_j = 3/2$ -state should be forbidden, but non-perfect polarization and misalignment in the magnetic field lead to an excitation of this state.

The width of the transition to the $m_j = 3/2$ -state is 1.56 MHz according to the fit. This value is a factor 1000 larger than the natural linewidth according to section 3.1. Reasons for the broadening are Doppler broadening which is about 20 kHz at these temperatures and an inhomogeneous magnetic field across the sample. Different g-factors for ground- and Rydberg-state thus lead to spatially dependant resonance frequencies.

For measuring the long time stability of the laser system the scan range was limited around the $m_j = 5/2$ transition to get a higher resolution. For a time of three hours this measurement was repeated once a minute. The resulting spectra are shown in figure 3.26 a) in a

colormap. For clarity the relative drift of the maxima is plotted in figure 3.26 b). For the

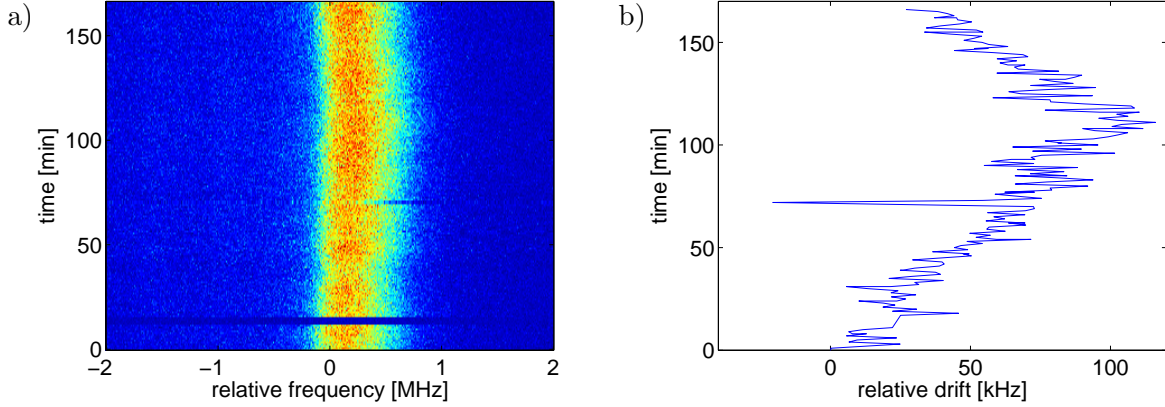


Figure 3.26.: Measurements to observe the stability of the laser system. a) shows a colorplot of the transition to the $44D_{5/2}, m_j = 5/2$ -state. In b) the maxima are extracted to clarify the result.

first 110 min of the measurement a linear drift with a maximum relative change of 100 kHz is observable. After this time a linear drift in exactly the other direction occurs.

The source of this drift is not clear. One reason might be a drift of the magnetic field and therefore a shift in the energy levels. In measurements so far such a drift could not be observed, as stability of the laser system actually used in this setup is not high enough. The second cause of the drift might be the slow branch of the feedback loop regulating the piezo element. A wrong setting might cause a oscillation around the zero crossing of the error signal with a large time-constant.

Spectroscopy on the 35S-state

Spectroscopy on a S-state provides one great benefit in contrast to spectroscopy on a D-state. As the g-factor for both the ground-state and the Rydberg-state are equal, the spectrum is not influenced by the magnetic field, enabling a better resolution. The frequencies and polarizations were again chosen according to the scheme in appendix C.

A spectrum obtained from spectroscopy on the $35S_{1/2}$ -state is shown in figure 3.27.

The fit yields a width of 30 kHz, still larger than the natural linewidth of 10 kHz. Besides the laser linewidth there are still additional mechanisms contributing to the linewidth. The temperature at which the spectrum was taken was $1.3 \mu\text{K}$ resulting in a Doppler broadening of 20 kHz. Due to the pulsed excitation with a pulse duration of $100 \mu\text{s}$ the Fourier-width of the pulse has to be taken in consideration, which is 8 kHz for this duration [57]. Accordingly the measured linewidth is a convolution of all these contributions. The combined linewidth of both lasers can therefore be still more narrow than 30 kHz and is in the desired order of magnitude.

In comparison to the spectra obtained with the Rydberg laser system used so far in this experiment, the measured linewidth of this transition is smaller by a factor of two.

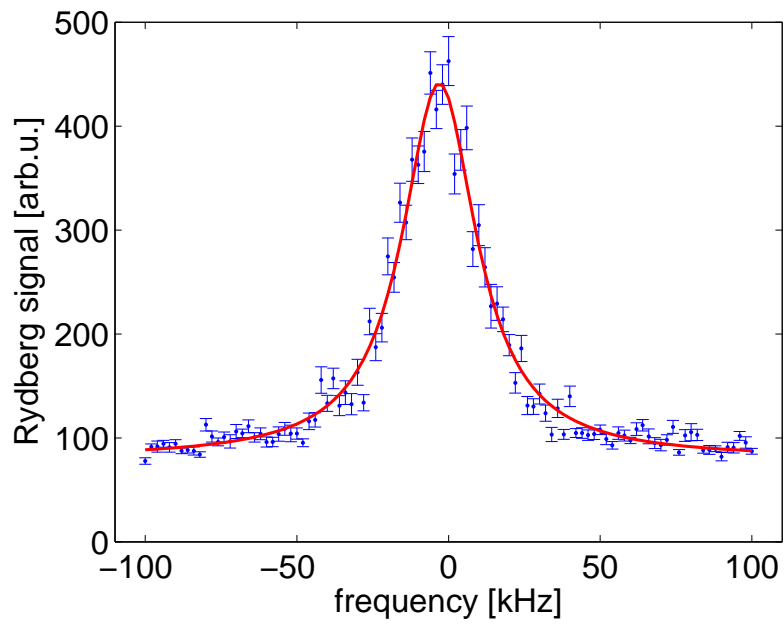


Figure 3.27.: Rydberg spectrum of the 35s state

4. Rydberg box

Like already mentioned in chapter 2 the Rydberg experiments are performed in a special metallic box. This chapter discusses the design and the construction of this box and describes simulations concerning the electric fields which can be generated in this box.

4.1. Rydberg atoms in electric fields

To manifest the need for an accurate electric field control, this section introduces into the influence of electric fields on Rydberg atoms. The first section describes the shift of the energy-levels due to small electric fields, while the second section concentrates on the ionization of Rydberg-atoms by strong electric fields.

4.1.1. Stark-shift of Rydberg states

The effect on the atomic levels of Rydberg atoms exposed to weak electric fields can be treated quantum-mechanically by applying perturbation theory. According to standard textbooks, an approximation for the new eigen-energies of a system influenced by a perturbation \hat{V} is given by

$$E_n = E_{0,n} + \langle n | \hat{V} | n \rangle + \sum_{m, m \neq n}^{\infty} \frac{|\langle n | \hat{V} | m \rangle|^2}{E_{0,n} - E_{0,m}} + \mathcal{O}(\hat{V}^3), \quad (4.1)$$

where E_n is the eigen-energy of state $|n\rangle$ in the perturbed system, while $E_{0,n}$ is its eigen-energy without perturbation. The sum in the second order term runs over all other states m .

For a Rydberg atom placed in a weak, homogeneous electric field \mathbf{E} with potential $\Phi = -|\mathbf{E}| \cdot z$ the perturbation for the electron charged with $-e$ is given by

$$\hat{V} = e|\mathbf{E}|z. \quad (4.2)$$

When putting this into equation 4.1 a distinction between two different cases is necessary. For Rydberg atoms in low l-states (s,p,d,f) degeneracy of the unperturbed energy-levels is lifted, as the quantum-defect depends on the quantum-number j . In the case of $l \geq 4$ on

the other hand, the unperturbed energy-levels are degenerate.

Considering the first case, the first order term will give no contribution since \hat{V} is an antisymmetric function and thus only the expectation value of states with different parity leads to a finite value. Hence the main energy shift is caused by the second order term, due to a coupling of different Rydberg states. The energy shift compared to the unperturbed case is therefore a quadratic function of the applied electric field, leading to the name quadratic Stark-effect.

However, degeneracy of the eigenstates, like it occurs for high l-states, leads to admixtures having a permanent electric dipole-moment. In this case the first order term yields a finite value and gets predominant, the energy levels are shifted linearly with the strength of the electric field.

There is a simple intuitive picture describing these two different behaviors. In the non-degenerate case the electric field moves the electron's probability density with respect to the position of the core, causing an induced dipole-moment $\mathbf{p}_{ind} = \alpha\mathbf{E}$. The strength of this effect scales with the polarizability α , leading to a large effect for the weakly bound Rydberg electron. The resulting potential energy of the induced dipole-moment is $U_{pot} = -\mathbf{p}_{ind}\mathbf{E} = -\alpha\mathbf{E}^2$, showing also a dependence on the electric field squared. In contrast, the potential energy of a permanent dipole-moment $U_{pot} = -\mathbf{p}_{perm}\mathbf{E}$ is just linearly depending on the electric field.

4.1.2. Field ionization of Rydberg atoms

When the strength of the electric field is raised to high values, the perturbative approach is not valid anymore. Instead the problem can be considered in a classical picture.

The potential causing the attractive force between the outer electron and the core of the Rydberg atom is of the Coulomb-type, given by

$$V_{\text{Coulomb}} = -\frac{e^2}{4\pi\epsilon_0 r}. \quad (4.3)$$

A homogeneous electric field with strength E in z -direction causes a linear potential

$$V_{\text{field}} = -eEz. \quad (4.4)$$

The Rydberg electron thus feels an effective potential consisting of the sum of these two potentials

$$V_{\text{eff}} = -\frac{e^2}{4\pi\epsilon_0 r} - eEz \quad (4.5)$$

In figure 4.1 a) the different potentials are plotted, showing a saddlepoint in the effective potential at the position

4. Rydberg box

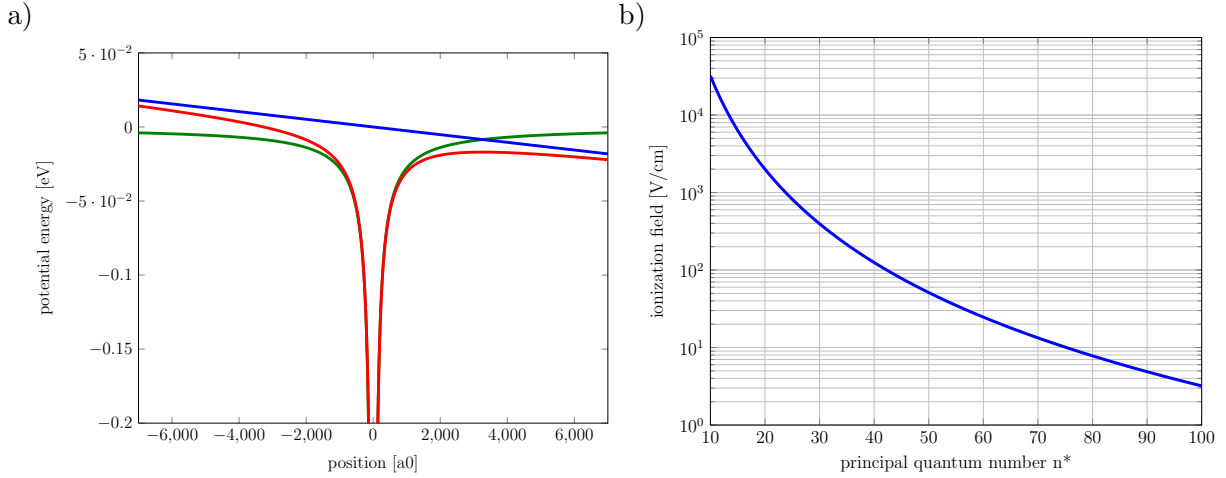


Figure 4.1.: Classical view on Rydberg ionization. An applied homogeneous electric field (blue) modifies the potential seen by the electron (green). The resulting effective potential (red) exhibits a saddlepoint at a certain position. Electrons of Rydberg atoms with a binding energy lower than this saddlepoint are not bound anymore, resulting in ionization of the atom. b) shows the dependence of the required field strength for a Rydberg atom with quantum number n^* .

$$z_{\text{saddle}} = \sqrt{\frac{e}{4\pi\epsilon_0 E}}. \quad (4.6)$$

The electron is only bound to the Rydberg atom, as long as its binding energy is higher than the energy of the saddlepoint. Otherwise the electron can cross the barrier and escape. Comparing binding energy E_{Ryd} and the energy at the saddlepoint $V_{\text{eff}}(z_{\text{saddle}})$ leads to the minimum electric field necessary to ionize a Rydberg atom. Following the condition

$$E_{\text{Ryd}} \stackrel{!}{\geq} V_{\text{eff}}(z_{\text{saddle}}) \quad (4.7)$$

the required electric field to ionize a Rydberg atom with effective quantum number n^* is

$$|\mathbf{E}| \geq \frac{\pi\epsilon_0 R_{\text{Ryd}}^2}{e^3 n^{*4}}. \quad (4.8)$$

Depending on the effective quantum number the electric field necessary for ionizing a Rydberg atom is depicted in figure 4.1. With decreasing quantum number the required field strength increases, as the electron is bound stronger to the atom. Nevertheless field strengths in the order of $\frac{\text{kV}}{\text{cm}}$ or even lower are sufficient for ionizing Rydberg atoms.

4.2. Design of the experiment box

With the knowledge regarding Rydberg atoms in electric fields obtained in chapter 4.1, a metallic box was designed giving the opportunity to control the electric fields during the experiment.

One requirement demanded for this box is a high electric field-control along two special directions which also have an optical access. These fields yield the opportunity to shift the atomic energy levels. For not broadening the linewidth of the transition due to different Stark-shifts, direction and strength of the applied electric field should deviate by less than one percent across the atomic cloud.

Along the third direction the electric fields for ionization of Rydberg-atoms should be applied. Also for this field a homogeneity across the cloud is requested, giving the opportunity for state-selective ionization. For subsequent ion detection both a multi-channel-plate (MCP) and a channeltron have to be mounted to this experiment chamber. To obtain good results, especially in the case of working with single atoms and photons, it is essentially required to have a high efficiency of detection events with these tools. Designs with similar goals were already successfully tested in various experiments [58, 59].

With this box a typical Rydberg experiment will have the following sequence: First the atoms are loaded from the MOT into the magnetic trap via the magnetic transport. After cooling a desired electric field is applied in the experiment box according to the planned experiment. After excitation of the Rydberg atoms, a high electric field is ramped up to ionize the excited Rydberg atoms. Subsequently the ions are detected by the ion detectors providing information about the Rydberg-atoms.

Besides these desired features, some constraints have to be taken in consideration. These are given by the space inside the glass cell and the position of the atom cloud, defined by the magnetic fields of the QUIC-trap. In figure 4.2 the important dimensions which have to be maintained are illustrated. The coordinates indicated there are valid for the next sections.

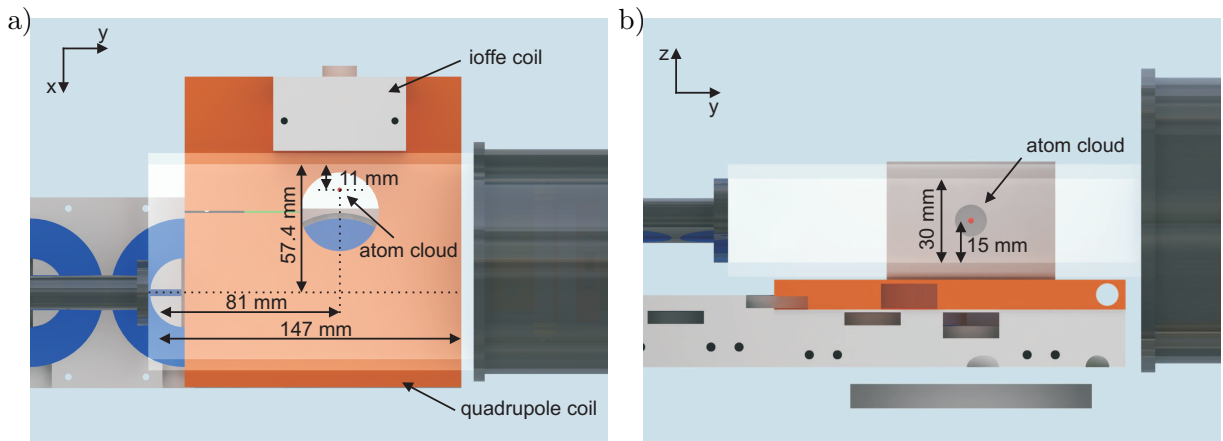


Figure 4.2.: Constraints limiting the possible geometries of the experiment chamber. View from top a) and side b) on the glass cell, where the chamber will be placed.

As illustrated in the view on the glass cell the size of the box in x-direction is limited by the position of the atom cloud and the magnetic transport. Due to the magnetic field of the Ioffe-coil the distance between atoms and wall of the glass cell is only 11 mm in y-direction. Additionally, the extension of the box has to be small enough in this direction to not block the route of the atoms during the magnetic transport.

In y-direction dimensions are not restricted so strictly, giving the opportunity to mount both MCP and channeltron on this axis. Finally, the height of the chamber is limited by the height of the glass cell which is 30 mm. Additionally, in the upper and lower wall two aspheric lenses with a working distance of 9 mm have to be added.

Due to the magnetic fields, the atom cloud will have the shape of a cigar, with temperature dependant size. For the calculated trap frequencies and an upper temperature of $500 \mu\text{K}$ maximal sizes of 1 mm in x-direction and $500 \mu\text{m}$ in y- and z-direction can be estimated. At least within this volume the electric fields have to be homogeneous for not leading to broadening effects due to different energy-shifts of the Rydberg atoms.

4.2.1. Electric fields inside a metallic box

Before starting with detailed simulations for various geometries, the electric field inside a closed metallic box was calculated by the means provided by classical electrostatics.

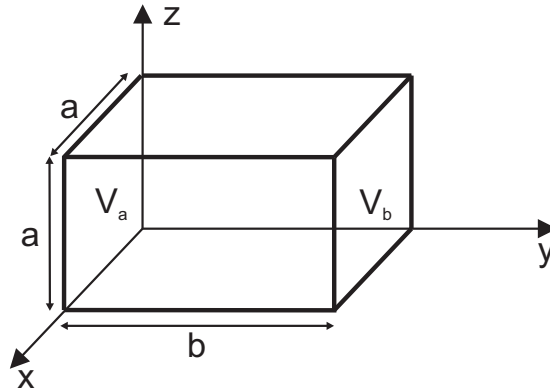


Figure 4.3.: Geometry used to calculate the electrical potential inside. The electrodes at $y = 0$ and $y = b$ can be put on a potential V_a and V_b , respectively. In the calculations $b/a = 1.6$ was chosen, corresponding to the realistic scale of the design.

In the calculations a cuboid shaped box with an aspect ratio of 1.6 is assumed (figure 4.3). Each of the six surrounding electrodes is individually addressable to generate fields inside the box. By applying a voltage on the electrodes, boundary conditions for the electric potential inside the box are defined. In this case the potential inside the box can be calculated by using Dirichlet boundary condition [60], given by

4. Rydberg box

$$\begin{aligned}\Phi_0(\mathbf{r}) &= \Phi(\mathbf{r})|_b \\ \Delta\Phi(\mathbf{r}) &= -4\pi\rho(\mathbf{r}).\end{aligned}\tag{4.9}$$

These equations connect the charge distribution $\rho(\mathbf{r})$ inside the chamber with the potential $\phi(\mathbf{r})$ and state that the potential at the border $\Phi(\mathbf{r})|_b$ is given by the potential of the metallic surrounding $\Phi_0(\mathbf{r})$.

Solving these conditions for this geometry is an exercise discussed in several electrodynamic textbooks. The solution for the potential inside the box is given by

$$\Phi(x, y, z) = \frac{16}{\pi^2} \sum_{m,n} \frac{\sin\left(\frac{m\pi x}{a}\right) \sin\left(\frac{n\pi z}{a}\right)}{mn} [V_a \sinh(\gamma_{mn}(b-y)) + V_b \sinh(\gamma_{mn}y)],\tag{4.10}$$

where the sum is running over all integer numbers m, n and $\gamma_{mn} = \frac{\pi}{a} \sqrt{m^2 + n^2}$.

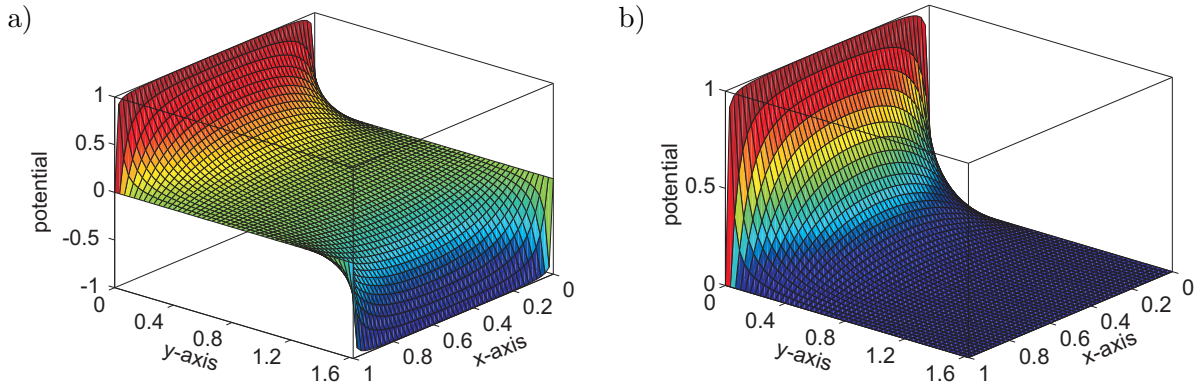


Figure 4.4.: Electric potential inside the box illustrated in figure 4.3 for the cases $V_a = -V_b = 1$ (a) and $V_a = 1, V_b = 0$ (b). Both times the potential is shown in the plane $z = \frac{a}{2}$.

Figure 4.4 shows the electric potential inside the box calculated by this formula for the cases $V_a = -V_b = 1$ (a) and $V_a = 1, V_b = 0$ (b). It is important to note that in both cases the potential in the plane $z = \frac{a}{2}$ is shown.

As the electric field is connected to the electric potential by $\mathbf{E} = -\text{grad}\Phi$, only a potential with a constant slope leads to a homogeneous potential. In the cases taken in consideration however, the potential shows a curvature resulting from the grounded surrounding electrodes. The resulting electric field is therefore not homogeneous across the complete chamber.

However, in the case of antisymmetric voltages applied on the opponent plates the potential is linear in the area around the center of the box. Thus the electric field is homogeneous at

this position. Compared to a simple plate capacitor with the same conditions the strength of the field in the center is, of course, weaker.

In case of only one charged side the potential is curved across the complete area, i.e. the electric field is not homogeneous at all.

From this calculation one can draw the conclusion that for obtaining a electric field as homogeneous a possible inside such a metallic box, one has to apply the voltage anti-symmetrically on the opposite electrodes.

4.2.2. Design of the box

After various simulations (see section 4.2.3) a geometry was found, satisfying the requirements as best as possible. The technical drawing of the final design as well as the actual construction build by the institute mechanical workshop are shown in figure 4.5.

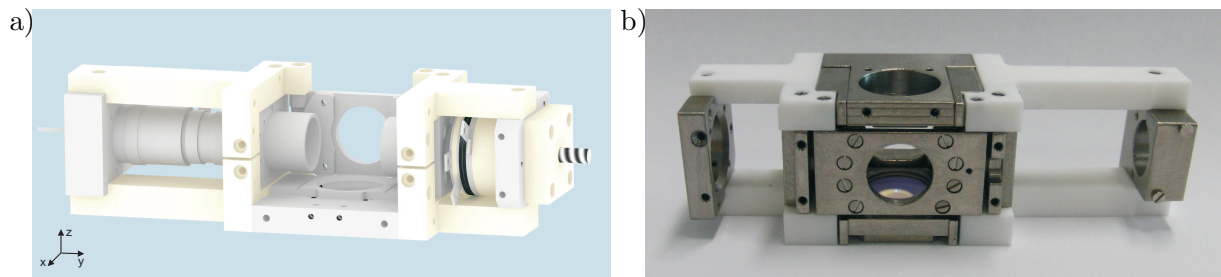


Figure 4.5.: Engineering drawing a) and picture of the experiment chamber b)

All the metallic parts, such as the electrodes and the mounts for channeltron and MCP are made from titanium. In contrast to stainless steel, which would be also an appropriate material for UHV applications, it has the big advantage of being not magnetizable. This property is important to prevent influences on the atoms trapped in the magnetic field of the QUIC-trap.

To electrically isolate all electrodes from each other, they are separately mounted on MACOR-spacers. This is a non-porous glass-ceramic which can be mechanically machined, providing therefore an ideal isolator for UHV applications.

The upper and lower electrode simultaneously serve as holders for the aspheric lenses providing high optical resolution in this direction. For the lower lens the holder is shown more detailed in figure 4.6

To improve field homogeneity and to shield dielectric surfaces all apertures in the electrodes are covered by thin titanium wires with a diameter of $50\ \mu\text{m}$. These wires are tightened with braces which are screwed to the electrodes. Tests ensured that the wires do not move, when a high voltage is applied to the electrode, as this would have negative impact on the high resolution imaging through the apertures. The purpose of these wires is to keep the voltages required for a certain electric field low. Another task is to screen surface charges of the lenses which may occur when a voltage is applied to the surrounding electrode.

4. Rydberg box

Not shown in the pictures of the experiment chamber are the connections to apply voltages to the electrodes.

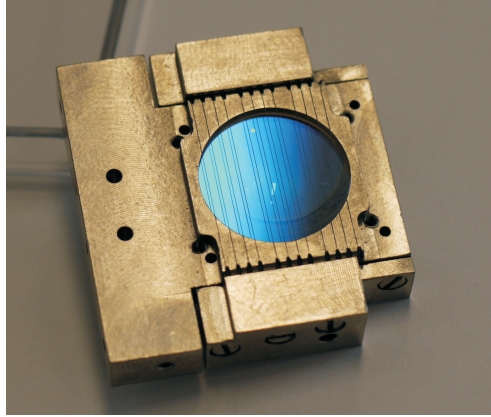


Figure 4.6.: Detailed view on the lens holder. The aperture for the lens is covered by thin titanium wires with a diameter of $50\ \mu\text{m}$. Are used to screen surface charges which may occur on the lens, when a voltage is applied to the surrounding electrode.

4.2.3. Simulations of the electric field control

For finding a suitable design for the experiment box the software SIMION was used, specially designed to calculate static electric fields and trajectories of charged particles by the finite element method. The possibility to import CAD-files allows to do simulations on any geometry. For all simulations the resolution was limited to $100\ \mu\text{m}$ due to processing power and the amount of produced data.

Simulations of electric fields used to shift the energy levels

The result of a simulation for an electric field inside the box which could be used for Stark-shifting the energy levels of the Rydberg atoms in figure 4.7. In this simulation a potential of $1\ \text{V}$ was applied to the field plate next to the wall of the glass cell and a potential of $-1\ \text{V}$ to the opposite electrode. As it is impossible to illustrate a three-dimensional electric field in a three-dimensional space, these plots show cuts through the center of the chamber in x-direction (a), b)) and z-direction (c), d)). From the data obtained by the simulation two quantities were calculated. On the one hand the absolute value of the electric field and on the other hand the absolute value of the angle between the electric field-vector and its component in x-direction (the direction of the desired field). Using this method to illustrate electric fields, a homogeneous electric field has a constant absolute value and field-vector points exactly in the desired direction.

In comparison with the size assumed for the atomcloud in the experiment the area illustrated in plots of figure 4.7 is much larger. The area of interest has like described above a maximum size only of $500\ \mu\text{m}$ in x- and z-direction and of $1\ \text{mm}$ in y-direction around the center. On this scale the strength is constant with a deviation of less than 1% and the direction of the electric field varies by less than 0.3 degrees. This accuracy is, however, sufficient for our experiments.

To achieve more homogenous fields, one must only use two electrodes mounted face by face. This solution is not desired in our setup, as it does not allow to screen the dielectric surfaces of the glass cell.

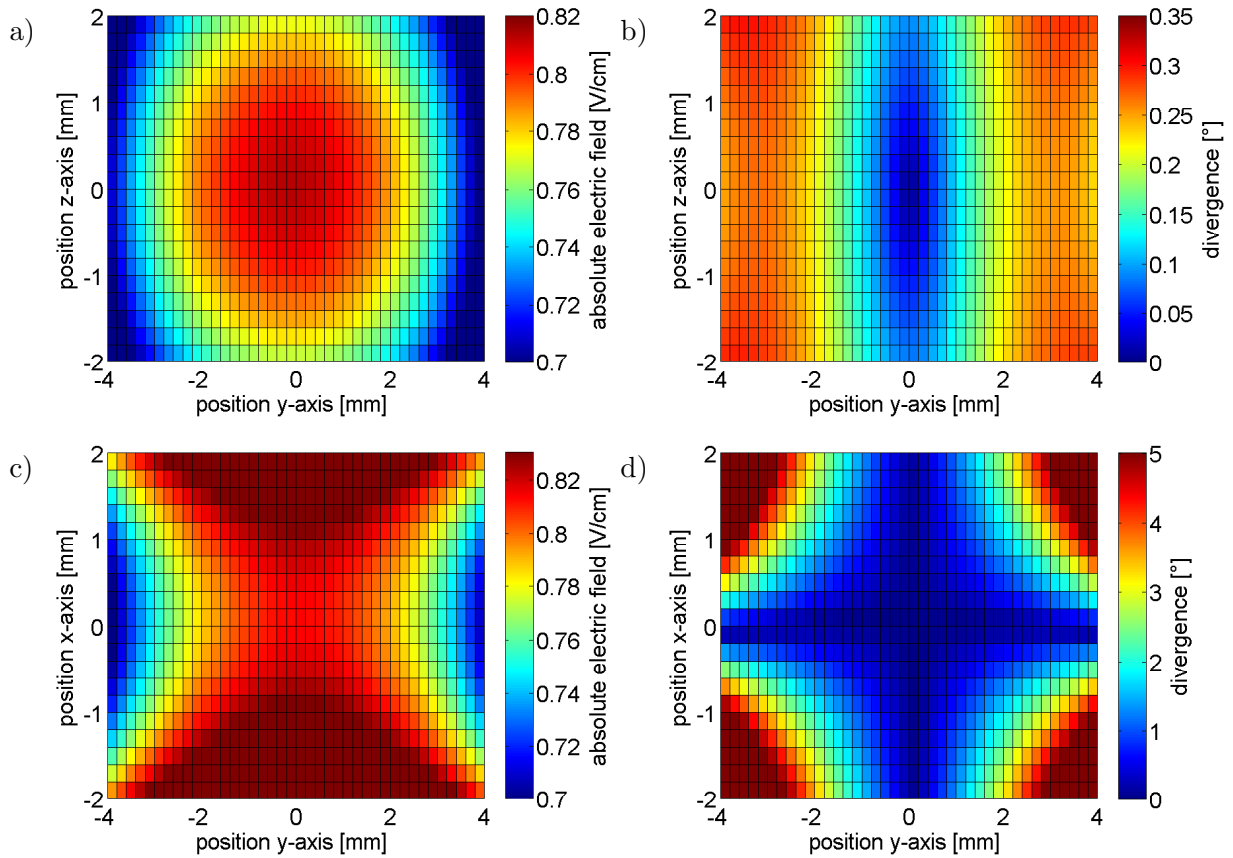


Figure 4.7.: Simulated electric fields resulting from a potential of 1 V applied to the field plate next to the wall of the glass cell and of -1 V on the opposite electrode. The images in the upper row are obtained by a cut through the center in x-direction, the one in the lower row by a cut through the center of the box in z-direction. For informations about the direction of the electric field absolute value (left) and angle (right) are plotted separately.

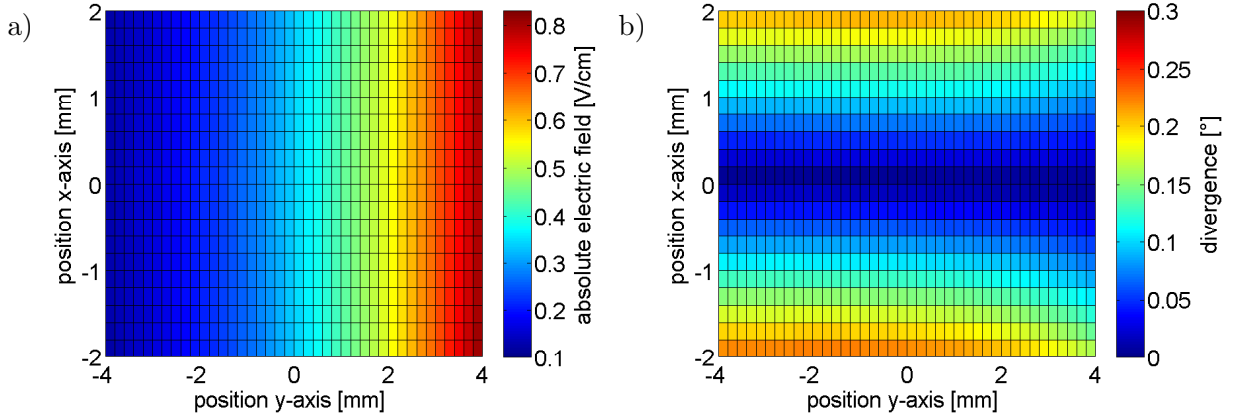


Figure 4.8.: Simulated electric fields resulting from a potential applied to the field plate next to the channeltron, cut through the center of the chamber in z-direction.

Simulations of electric fields used to ionize Rydberg atoms

This section deals with the results of the simulations concerning the ionization of Rydberg atoms. For ionization and detection of Rydberg atoms excited in an experiment an electric field pointing in the direction of MCP or channeltron, respectively, is ramped up. If the strength of the electric field in the center is high enough, Rydberg atoms are ionized and the ions are accelerated towards MCP or channeltron where they are detected. To prevent crosstalk with MCP and channeltron only the field plate on the opposite side of the chamber is put on a potential.

Figure 4.8 shows the electric fields for this situation. According to the calculation in section 4.2.1 the strength of the electric field is not constant, even on a small range. However, for the desired state-selective ionization this is required.

To determine if state-selective ionization of Rydberg atoms is nevertheless possible with this geometry, the minimum and maximum value of the strength of the electric field over the area of the atomic cloud was calculated. For ionizing a certain state with quantum number n , the minimum electric field has to be equal to the corresponding value obtained from equation 4.8. If the resulting maximum electric field across the volume of the cloud is smaller than the field required for ionization of the subsequent state, state-selective ionization is possible.

To illustrate this, figure 4.9 a) shows both the difference between the maximum and minimum electric field in the volume of the atom cloud when the minimum field is required to ionize a certain state and the difference in the required fields for ionization of neighbored states. The possibility of state-selective ionization is given, when the difference between the electric fields inside the volume is smaller than the difference between the electric fields required to ionize neighboring states. From the figure it becomes clear, that the size of the atom cloud in y-direction determines the range on which state-selective ionization is possible. For a diameter of $200\ \mu\text{m}$ in this direction state-selective ionization over the range from $n = 15$ to $n = 70$ is possible, whereas for a diameter of $400\ \mu\text{m}$ and above $n = 40$

4. Rydberg box

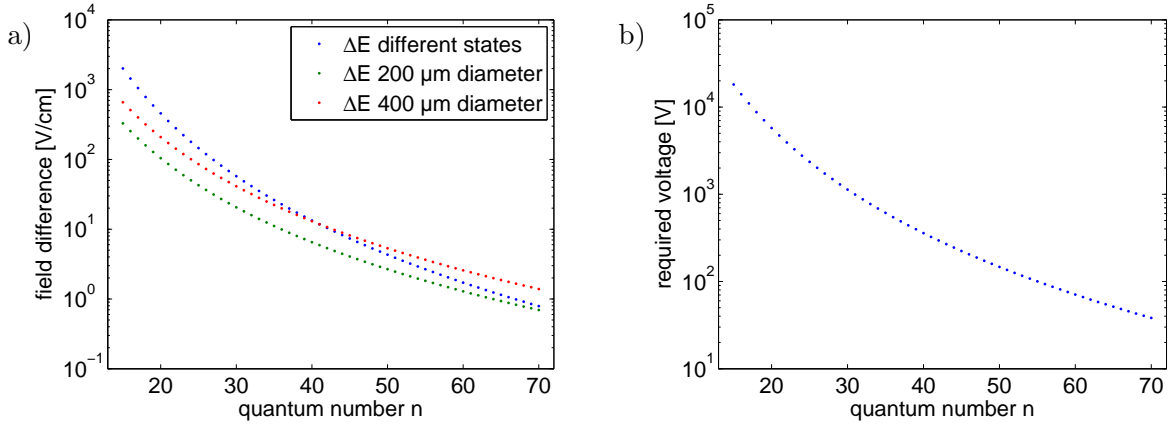


Figure 4.9.: Investigation for the opportunity of state-selective ionization (a)) and voltage required to ionize a certain Rydberg state (b)).

multiple states are ionized.

For this calculation one should however keep in mind, that truly for the Alkalis (except Hydrogen) each Rydberg state has to be described by its effective quantum number n^* . Therefore not only integer numbers are allowed as quantum number, resulting in shifted differences between the electric fields required for ionizing neighbored states. Moreover, the ionization fields calculated by the introduced model do not fit exactly as the tunnel-effect neglected in this classical approximation washes out the differences between different states.

Additionally, figure 4.9 shows the voltages which have to be applied to the electrode to ionize a certain state. As for small quantum number below $n = 25$ very high voltages in the range of 10 kV are required, these states might be not accessible by ionization.

Especially in the case of working with single Rydberg atoms a high probability of detection is absolutely necessary. Both the probability of hitting the surface of the MCP or channeltron and the spatial distribution of Rydberg-atoms ionized in the center of the box was ionized to verify this. Therefore 1000 single charged ions with the mass of a Rubidium-atom were equally distributed across the volume of the atom cloud. Then the trajectories of the ions were simulated with the SIMION-software, assuming a field strength required for ionization of the $n = 45$ Rydberg-state. From the trajectories the number and the positions of the ions hitting the MCP/channeltron were determined (figure 4.10).

The hit-points of the ions are distributed across the complete surface of the channeltron which has a diameter of 6.8 mm. Accordingly the detection area of the larger MCP (diameter 13 mm is not completely filled out. The stripes in the hit-statistic are images of the wires stretched across the electrode. These are also responsible for a efficiency of hitting ions of only 73%. As the diameter of the wires was 100 μm instead of 50 μm in the simulations, the efficiency will increase in the experiment. However, one has to keep in mind, that the probability of ions hitting the surface of MCP or channeltron is not equal to the detection efficiency in the experiment as not every hitting ion is counted by the detectors.

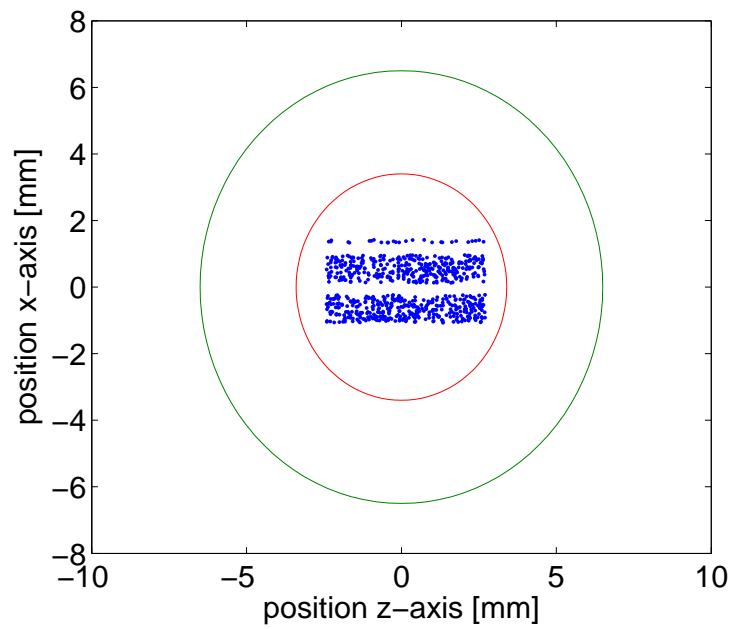


Figure 4.10.: Simulated hit statistic of ions on MCP and channeltron, respectively. For the simulation 1000 ions were equally distributed across the estimated maximum size of the atom cloud.

5. Summary and Outlook

In the scope of this thesis the setup of a new apparatus for experiments involving Rydberg atoms in ultra-cold atomic gases was described. The focus was thereby put on the setup of a laser-system with high stability enabling precise excitation of Rydberg-atoms via a two-photon transition. The second part treated the construction of a chamber providing high electric field control and the ability for ion-detection with high efficiency.

For the setup of the laser-system two commercial lasers running at a wavelengths of 780 nm and 480 nm with a specified short time stability of 100 kHz measured on a timescale of 5 μ s have been used. To improve this stability the lasers were stabilized by the Pound-Drever-Hall technique to an external cavity with excellent stability. This results from mounting the mirrors on a temperature stabilized spacer made from ultra-low-expansion glass (ULE). The free spectral range of 1.5 GHz and the Finesse of 1600 result in a steep error signal with a capture range of 590 kHz. Optimizing the feedback of a fast PID-controller (Toptica FALC) enabled the reduction of the linewidth on a long timescale. By locking the lasers on modulated sidebands with variable frequencies between 60 MHz and 720 MHz both lasers can be scanned across the full free spectral range of the cavity.

To characterize both long-time stability and linewidth several techniques were employed. From a beatnote with a further laser stabilized to a Rubidium cell by DAVLL-spectroscopy a maximum linewidth of 40 kHz on a timescale of 700 ms was derived for the 780 nm laser. Tracking the center frequency of the beatnote for 24 hours led to relative stability of at least 600 kHz during this time. Further measurements clarified that this drift is completely caused by the reference laser.

With an self-heterodyne interferometer the stability of both lasers was measured on a timescale of 52 μ s. Thereby the linewidth was below the resolution limit of 20 kHz.

Finally, the new laser system was used for Rydberg-spectroscopy of ultra-cold atoms in the existing setup. Spectroscopy of the $44D$ -state shows a drift of approximately 100 kHz on the timescale of 1 hour, which is caused by magnetic field drifts. With spectroscopy on the $35S$ -state which is independent of the magnetic field a transition linewidth of 30 kHz was measured, setting the lowest limit on the laser linewidth so far. At this level, effects such as Doppler broadening due to atomic movement and Fourier-transform limited broadening due to the finite pulse duration dominate the linewidth. From this we can conclude that the achieved laser linewidth approaches the natural lifetime of Rydberg states and for all practical purposes is not a limitation in ongoing and planned experiments any more. Even more precise characterization will become possible in the near future, when a second identical setup becomes available for direct comparison.

Due to the small linewidth and the negligible drift over time achieved with the new laser-

system it is currently being used in the already existing Rydberg-experiment. The improved performance of the new system is of great benefit for the on-going experiments on Rydberg-dressing in Bose-Einstein condensates requiring high stability in the complete experiment [61].

The second project, which was completed during this thesis, was the construction of a box providing high electric field control, high optical resolution and high detection efficiencies during the experiment. The design had to be adapted to the constraints set by the inside dimensions of the glass cell and the magnetic transport. The result is a small metallic box existing of six separately addressable electrodes. By applying electric potentials to the electrodes, electric fields inside the chamber can be generated. The exact design of these electrodes was optimized with the help of a software for finite element simulations of electric fields (SIMION), with the goal being the realization of extremely homogeneous fields over the volume occupied by the ultra-cold atoms.

For the detection of Rydberg-atoms a multi-channel plate and a channeltron are mounted to the chamber. This allows detection of Rydberg-atoms by ionization and subsequent ion-detection. High detection efficiencies offer the feasibility for single ion detection. The guiding of ions from the atomic sample to the detectors via applied fields was simulated in detail and various ways to improve the guiding fields were found.

Concerning the setup of the complete apparatus the whole vacuum chamber is assembled so far. The starting point of the experiment, a magneto-optical trap, has already been realized. Currently the magnetic transport from the loading region to the experiment box is being finalized. In particular, problems with too much heat being generated by the electromagnets are currently being resolved. After the magnetic transport has been optimized, and high atom numbers can be reliably achieved in the experiment area, we will install the Rydberg-experiment box discussed in this thesis. Once all these components are in place, the envisioned Rydberg-experiments will begin.

The first of these experiments is the realization of a single-photon absorber based on the Rydberg blockade effect [16]. To reach this, a Rydberg atom is excited by the described two-photon process. In the absence of any decoherence the Rydberg-atom in the blockade sphere would undergo enhanced Rabi oscillations and would thereby be able to continuously absorb and re-emit photons from and into the two excitation laser fields. For the implementation of a single-photon absorber one therefore has to prevent the Rabi oscillations. This can be achieved by an artificial dephasing, coupling the addressable Rydberg-state in the superatom-model to the single-excitation dark-states. In this case only one photon of the light field couples to the atoms and is absorbed. With an EIT-scheme or by ionization and single-ion detection this photon can be detected afterwards. Until now simulations on this topic were started, showing that inhomogeneous shifting of the atomic levels leads to a desired dephasing, suppressing the collective Rabi oscillations.

A. Modematching to the cavity

The ULE-cavity consists of a planar mirror with a radius $R_1 = \infty$ and a concave mirror with a radius $R_2 = -500$ mm (the negative sign results from definition for a concave mirror) arranged in a distance $d = 100$ mm like shown in figure A.1.

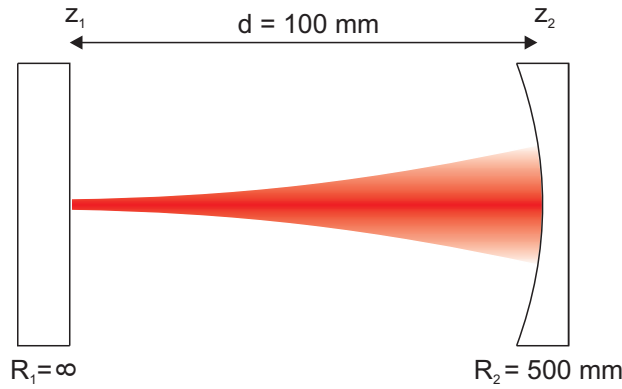


Figure A.1.: Dimensions of the used ULE-cavity defining the required Gaussian beam.

According to equation 3.23 it has to apply

$$R(z_1) = R_1 = z_1 + \frac{z_R^2}{z_1} \quad (\text{A.1})$$

and

$$R(z_2) = R_2 = z_2 + \frac{z_R^2}{z_2}. \quad (\text{A.2})$$

From A.1 and $R(z_1) = \infty$ it follows $z_1 = 0$ and therefore $z_2 = d$. Thus the planar mirror has to be placed at the position of the waist. The constraint for the curvature at the second mirror leads to the Rayleigh range and the beam radius at the waist.

$$\begin{aligned} R(z_2) &= d + \frac{z_R^2}{d} \\ z_R^2 &= (R(z_2) - d) \cdot d \\ z_R &= 200 \text{ mm} \end{aligned}$$

The beam radius at the waist can be obtained by the relationship 3.22. The values are

$$w_{0,960} = 222,8 \text{ } \mu\text{m}$$

A. Modematching to the cavity

for 780 nm and

$$w_{0,960} = 247,2 \mu\text{m}$$

for 960 nm.

The frequency separation between the fundamental mode and higher order modes is given by equation 3.24, with $\xi(z) = \arctan\left(\frac{z}{z_R}\right)$.

With the parameters of the cavity the separation between modes of different order is

$$\Delta\nu_{1,1+1} = 220.6 \text{ MHz}$$

B. Electronics for scanning the laser

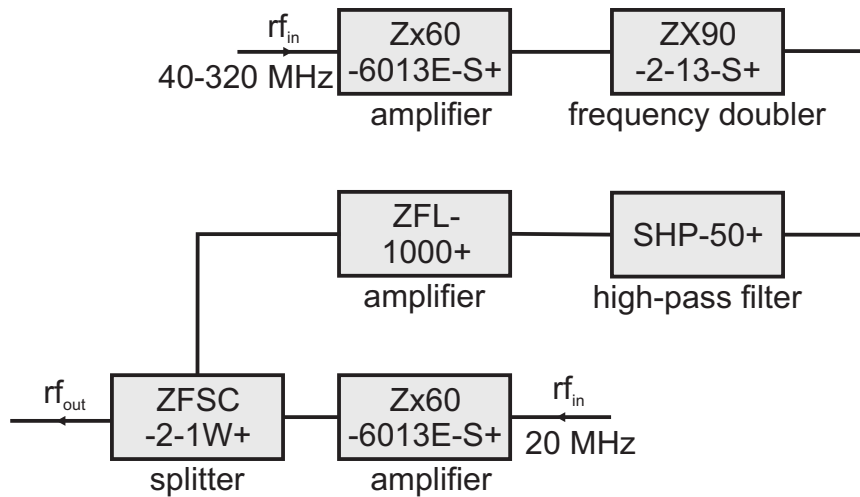


Figure B.1.: Used MiniCircuits components to scan the frequency of the DLpro

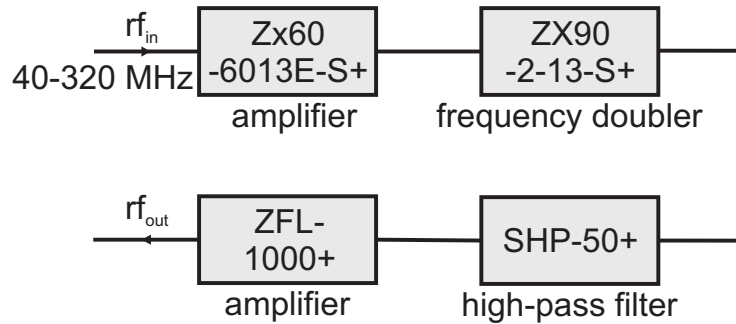


Figure B.2.: Used MiniCircuits components to scan the frequency of the TA-SHG

C. Excitation scheme for Rydberg excitation

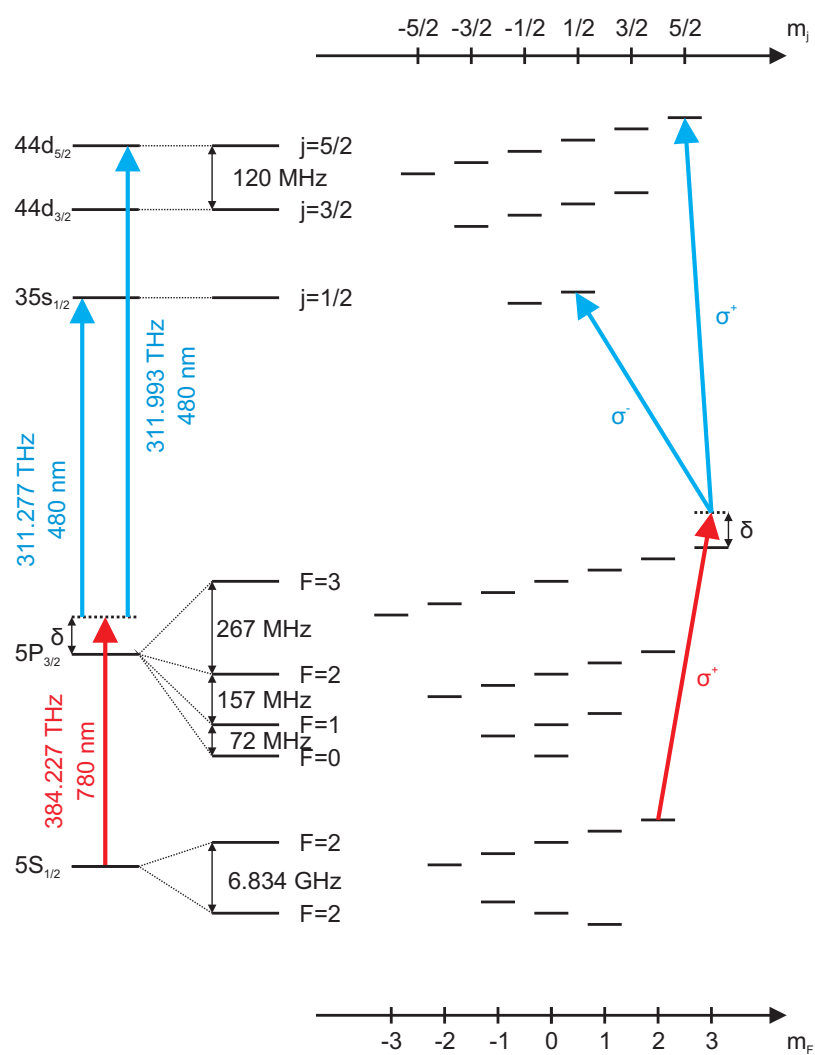


Figure C.1.: Excitation scheme for Rydberg excitation into the $44d_{5/2}$ -state in a magnetic field.

Bibliography

- [1] I. Martinson and L. J. Curtis. *Janne Rydberg - his life and work*. Nucl. Instr. Meth. Phys. Res. Sec. B, 235, 2005.
- [2] M. Saffman, T. G. Walker, and K. Mølmer. *Quantum information with Rydberg atoms*. Rev. Mod. Phys., 82(3):2313–2363, Aug 2010.
- [3] J. I. Cirac and P. Zoller. *Quantum Computations with Cold Trapped Ions*. Phys. Rev. Lett., 74, 1995.
- [4] P. Neumann, R. Kolesov, B. Naydenov, J. Beck, F. Rempp, M. Steiner, V. Jacques, G. Balasubramanian, M. L. Markham, D. J. Twitchen, S. Pezzagna, J. Meijer, J. Twamley, F. Jelezko, and J. Wrachtrup. *Quantum register based on coupled electron spins in a room-temperature solid*. Nature Physics, 6:249–253, 2010.
- [5] D. Loss and D. P. DiVincenzo. *Quantum computations with quantum dots*. Phys. Rev. A, 57, 1998.
- [6] R. Feynman. *Simulating physics with computers*. International Journal of Theoretical Physics, 21:467–488, 1982.
- [7] D. Jaksch, J. I. Cirac, P. Zoller, S. L. Rolston, R. Côté, and M. D. Lukin. *Fast Quantum Gates for Neutral Atoms*. Phys. Rev. Lett., 85(10):2208–2211, Sep 2000.
- [8] M. D. Lukin, M. Fleischhauer, R. Cote, L. M. Duan, D. Jaksch, J. I. Cirac, and P. Zoller. *Dipole Blockade and Quantum Information Processing in Mesoscopic Atomic Ensembles*. Phys. Rev. Lett., 87(3):037901, Jun 2001.
- [9] V. Vuletic. *Quantum networks: When superatoms talk photons*. Nature Physics, 2:801–802, 2006.
- [10] K. Singer, M. Reetz-Lamour, T. Amthor, L. Gustavo Marcassa, and M. Weidemüller. *Suppression of Excitation and Spectral Broadening Induced by Interactions in a Cold Gas of Rydberg Atoms*. Phys. Rev. Lett., 93, 2004.
- [11] R. Heidemann, U. Raitzsch, V. Bendkowsky, B. Butscher, R. Löw, L. Santos, and T. Pfau. *Evidence for Coherent Collective Rydberg Excitation in the Strong Blockade Regime*. Phys. Rev. Lett., 99, 2007.
- [12] Y. O. Dudin, L. Li, F. Bariani, and A. Kuzmich. *Observation of coherent many-body Rabi oscillations*. Nature Physics (Published online), 2012.

- [13] E. Urban, T. A. Johnson, T. Henage, L. Isenhower, D. D. Yavuz, T. G. Walker, and M. Saffman. *Observation of Rydberg blockade between two atoms*. *nature physics*, 5, 2009.
- [14] A. Gaetan, Y. Miroshnychenko, T. Wilk, A. Chotia, M. Viteau, D. Comparat, P. Pillet, A. Browaeys, and P. Grangier. *Observation of collective excitation of two individual atoms in the Rydberg blockade regime*. *Nature Physics*, 5:115–118, 2009.
- [15] Y. O. Dudin and A. Kuzmich. *Strongly Interacting Rydberg Excitations of a Cold Atomic Gas*. *Science*, 336, 2012.
- [16] J. Honer, R. Löw, H. Weimer, T. Pfau, and H. P. Büchler. *Artificial Atoms Can Do More Than Atoms: Deterministic Single Photon Subtraction from Arbitrary Light Fields*. *Phys. Rev. Lett.*, 107, 2011.
- [17] B. Zhao, K. Hammerer, M. Müller, and P. Zoller. *Efficient quantum repeater based on deterministic Rydberg gates*. *Phys. Rev. A*, 81, 2010.
- [18] Y. Han, B. He, K. Heshami, C.-Z. Li, and C. Simon. *Quantum repeaters based on Rydberg-blockade-coupled atomic ensembles*. *Phys. Rev. A*, 81, 2010.
- [19] H. Weimer, M. Müller, I. Lesamovsky, P. Zoller, and H. P. Büchler. *A Rydberg quantum simulator*. *Nature Physics*, 6:382–388, 2010.
- [20] R. Löw. *A versatile setup for experiments with Rubidium Bose Einstein condensates: From optical lattices to Rydberg matter*. PhD thesis, Universität Stuttgart, 2006.
- [21] R. Heidemann, U. Krohn, V. Bendkowsky, B. Butscher, R. Löw, and T. Pfau. *Rydberg Excitation of Bose-Einstein Condensates*. *Phys. Rev. Lett.*, 100, 2008.
- [22] R. Löw, H. Weimer, U. Krohn, R. Heidemann, V. Bendkowsky, B. Butscher, H. P. Büchler, and T. Pfau. *Universal Scaling in a strongly interacting Rydberg gas*. *Phys. Rev. A*, 80, 2009.
- [23] B. Butscher, J. Nipper, J. B. Balewski, L. Kukota, V. Bendkowsky, R. Löw, and T. Pfau. *Atom-molecule coherence for ultralong-range Rydberg dimers*. *Nature Physics*, 6:970–974, 2010.
- [24] J. Nipper, J. B. Balewski, A. T. Krupp, B. Butscher, R. Löw, and T. Pfau. *Highly Resolved Measurements of Stark-Tuned Förster Resonances between Rydberg Atoms*. *Phys. Rev. Lett.*, 108, 2012.
- [25] J. Nipper, J. B. Balewski, A. T. Krupp, S. Hofferberth, R. Löw, and T. Pfau. *Atomic Pair-State Interferometer: Controlling and Measuring an Interaction-Induced Phase Shift in Rydberg-Atom Pairs*. *Phys. Rev. X*, 2, 2012.

- [26] S. Jennewein. *Building an Apparatus for Cold Rubidium Rydberg Atoms*. Diploma thesis, Universität Stuttgart, 5. Physikalisches Institut, 2012.
- [27] M. Greiner, I. Bloch, T. W. Hänsch, and T. Esslinger. *Magnetic transport of trapped cold atoms over a large distance*. Phys. Rev. A, 63, 2001.
- [28] Matthias Theis. *Optical Feshbach Resonances in a Bose-Einstein Condensate*. PhD thesis, Leopold-Franzens-Universität Innsbruck, 2005.
- [29] H. J. Metcalf and P. van der Straten. *Laser Cooling and Trapping*. Springer, 1999.
- [30] T. Esslinger, I. Bloch, and T. W. Hänsch. *Bose-Einstein condensation in a quadrupole-Ioffe-configuration trap*. Phys. Rev. A, 58(4).
- [31] D. M. Brink and C. V. Sukumar. *Majorana spin-flip transitions in a magnetic trap*. Phys. Rev. A, 74(3).
- [32] W. Ketterle. *Evaporative cooling of trapped atoms*. Advances In Atomic, Molecular, and Optical Physics, 37, 1996.
- [33] I. I. Ryabtsev, I. I. Beterov, D. B. Tretyakow, V. M. Entin, and E. A. Yakshina. *Doppler- and recoil-free laser excitation of Rydberg states via three photon transitions*. Phys. Rev. A, 84, 2011.
- [34] F. Gounand. *Calculation of radial matrix elements and radiative lifetimes for highly excited states of alkali atoms using the Coulomb approximation*. Le Journal de Physique, 40(5):457–460, 1979.
- [35] I. I. Ryabtsev, I. I. Beterov, D. B. Tretyakov, and V. M. Entin. *Quasiclassical calculations of BBR-induced depopulation rates and effective lifetimes of Rydberg nS , nP and nD alkali-metal atoms with $n < 80$* . Phys. Rev. A, 79.
- [36] U. Krohn. *Universal scaling and coherence properties of an ultracold Rydberg gas*. PhD thesis, Universität Stuttgart, 2008.
- [37] J. D. Pritchard. *Cooperative Optical Non-linearity in a blockaded Rydberg Ensemble*. PhD thesis, Durham University, 2011.
- [38] D. A. Steck. *Rubidium 87 D Line Data*, 2010.
- [39] A. L. Schawlow and C. H. Townes. *Infrared and Optical Masers*. Phys. Rev., 112, 1958.
- [40] Xiaopei Chen. *Ultra-Narrow Laser Linewidth Measurement*. PhD thesis, Virginia Polytechnic Institute and State University, Blacksburg, Virginia, 2006.

- [41] S. Imanshi and U. Tanaka and S. Urabe. *Frequency stabilization of diode laser using dichroic-atomic-vapor laser lock signals and thin rb vapor cell*. Japanese Journal of Applied Physics, 44(9A), 2005.
- [42] C. Tresp. *Hochauflösende Fluoreszenzspektroskopie in Rubidium Dampfzellen*. Bachelor thesis, Universität Stuttgart, 5. Physikalisches Institut, 2010.
- [43] Anthony Siegman. *Lasers*. University Science Books, 1986.
- [44] B. E. A. Saleh and M. C. Teich. *Fundamentals of Photonics*. John Wiley and Sons, Inc., 2007.
- [45] R. W. P. Drever, J. L. Hall, F. V. Kowalski, J. Hough, G. M. Ford, A. J. Munley, and H. Ward. *Laser Phase and Frequency Stabilization Using an Optical Resonator*. Appl. Phys. B, 31:97–105, 1983.
- [46] E. D. Black. *An introduction to Pound-Drever-Hall laser frequency stabilization*. Am. J. Phys., 69:80–87, 2000.
- [47] J. Alnis, A. Matveev, N. Kolachevsky, Th. Udem, and T. W. Hänsch. *Subhertz linewidth diode lasers by stabilization to vibrationally and thermally compensated ultralo-expansion glass Fabry-Pérot cavities*. Phys. Rev. A., 77, 2008.
- [48] J. Bechhoefer. *Feedback for physicists: A tutorial essay on control*. Rev. Mod. Phys., 77:783–836, 2005.
- [49] R. Lang and K. Kobayashi. *Suppression of the Relaxation Oscillation in the Modulated Output of Semiconductor Lasers*. J. Quant. Elect., QE-12(3).
- [50] M. Nazarathy, W. V. Sorin, D. M. Baney, and S. A. Newton. *Spectral Analysis of Optical Mixing Measurements*. Journal of Lightwave Technologie, 7:1083, 1989.
- [51] J. Balewski. *Hochauflösende Photoassoziationsspektroskopie von Rydberg-Dimeren und Trimeren*. Diploma thesis, Universität Stuttgart, 5. Physikalisches Institut, 2009.
- [52] A. Kintchine. *Korrelationstheorie der stationären stochastischen Prozesse*. Mathematische Annalen, 1934.
- [53] G. di Domenico, S. Schilt, and P. Thomann. *Simple approach to the relation between laser frequency noise and laser line shape*. J. Apl. Opt., 49:4801–4807, 2010.
- [54] J. M. Reeves, O. Garcia, and C. A. Sackett. *Temperature stability of a dichroic atomic vapor*. Appl. Optics, 45(2).
- [55] H. Ludvigsen, M. Tossavainen, and M. Kaivola. *Laser linewidth measurements using self-heterodyne detection with short delay*. J. Opt. Commun., 155:180–186, 1998.

- [56] R. Heidemann. *Rydberg Excitation of Bose-Einstein Condensates: Coherent Collective Dynamics*. PhD thesis, Universität Stuttgart, 2008.
- [57] R. Scheunemann. *Lichtgebundene Atome: Manipulation kalter Atome in mesoskopischen optischen Gittern*. PhD thesis, Ludwig-Maximilians-Universität München, 2000.
- [58] D. B. Tretyakov, I. I. Beterov, V. M. Entin, I. I. Ryabtsev, and P. I. Chapovsky. *Investigation of Cold Rubidium Rydberg Atoms in a Magneto-Optical Trap*. JETP, 108(3), 2009.
- [59] A. Schwarzkopf, R. E. Sapiro, and G. Raithel. *Imaging Spatial Correlations of Rydberg Excitations in Cold Atom Clouds*. Phys. Rev. Lett., 107, 2011.
- [60] J. D. Jackson. *Classical Electrodynamics*. Wiley, New York, 2006.
- [61] J. Honer, H. Weimer, T. Pfau, and H. P. Büchler. *Collective Many-Body Interactions in Rydberg Dressed Atoms*. Phys. Rev. Lett., 105, 2010.

Danksagung

Abschließend möchte ich mich bei allen bedanken, die zum Gelingen dieser Arbeit beigetragen haben. Dies sind im Besonderen:

- Prof. Dr. Tilman Pfau, der mir die Möglichkeit gegeben hat meine Masterarbeit in diesem interessanten Bereich der Physik zu schreiben.
- Prof. Dr. Jörg Wrachtrup, der den Mitbericht für diese Arbeit und die damit verbundenen Mühen auf sich genommen hat.
- Dr. Sebastian Hofferberth, der in der Zeit der Masterarbeit mein Betreuer war und mir mit seiner großen Erfahrung immer mit Rat und Tat zur Seite stand.
- Dr. Robert Löw, der mir besonders bei der Konstruktion der Experimentbox mit seinen guten Ratschlägen sehr weitergeholfen hat.
- Michael Schlagmüller, Huan Nguyen, Stephan Jennewein und Hannes Gorniaczyk, die während meiner Masterarbeit als Doktoranden und Diplomanden am Experiment gearbeitet haben und von denen ich in verschiedenen Bereichen profitieren konnte.
- Jonathan Balewski, Alexander Krupp und Anita Gaj, die mir die Möglichkeit gegeben haben das neue Lasersystem an ihrer Apparatur zu testen.
- Die Mitarbeiter der mechanischen Werkstatt, insbesondere Herrn Kamella, für die aufgebrachte Mühe bei der Herstellung der Experimentbox.